ISPRS Journal of Photogrammetry and Remote Sensing 211 (2024) 372–391

Contents lists available at ScienceDirect

ISPRS Journal of Photogrammetry and Remote Sensing

journal homepage: www.elsevier.com/locate/isprsjprs

First retrieval of daily 160 m aerosol optical depth over urban areas using Gaofen-1/6 synergistic observations: Algorithm development and validation

Jiadan Dong [a], Tianhao Zhang [b,*], Lunche Wang [c], Zhengqiang Li [d], Man Sing Wong [e], Muhammad Bilal [f], Zhongmin Zhu [a,g], Feiyue Mao [h], Xinghui Xia [a], Ge Han [h], Qiangqiang Xu [i], Yu Gu [b], Yun Lin [b], Bin Zhao [j,k], Zhiwei Li [e], Kai Xu [l], Xiaoling Chen [a], Wei Gong [a]

[a] State Key Laboratory of Information Engineering in Surveying, Mapping and Remote Sensing, Wuhan University, Wuhan, China
[b] Joint Institute for Regional Earth System Science and Engineering, University of California, Los Angeles, USA
[c] School of Geography and Information Engineering, China University of Geosciences, Wuhan, China
[d] State Environmental Protection Key Laboratory of Satellite Remote Sensing, Aerospace Information Research Institute, Chinese Academy of Sciences, Beijing, China
[e] Department of Land Surveying and Geo-Informatics, The Hong Kong Polytechnic University, Hong Kong, China
[f] Center for Sustainability and the Global Environment, University of Wisconsin–Madison, WI, USA
[g] College of Information Science and Engineering, Wuchang Shouyi University, Wuhan, China
[h] School of Remote Sensing and Information Engineering, Wuhan University, Wuhan, China
[i] The Northwest Institute of Eco-Environment and Resources (NIEER), Chinese Academy of Sciences (CAS), Lanzhou, China
[j] State Key Joint Laboratory of Environmental Simulation and Pollution Control, School of Environment, Tsinghua University, Beijing, China
[k] State Environmental Protection Key Laboratory of Sources and Control of Air Pollution Complex, Beijing, China
[l] School Internet, Anhui University, Hefei, China

ARTICLE INFO

Keywords:
Daily 160 m AOD dataset
Retrieval algorithm
Gaofen-1/6 WFV
High resolution LSR modeling
Urban areas

ABSTRACT

The satellite-based aerosol optical depth (AOD), which can provide continuous spatial observations of aerosol loadings, is widely adopted to estimate atmospheric environmental quality and evaluate its risk for human health. However, current satellite-retrieved AOD products characterized by a comparatively coarse spatial resolution (≥1 km) can hardly analyze the structure of atmospheric pollution or its correlation with urban landscapes over populated urban areas. Existed studies have tried to address this deficiency by retrieving high-resolution AOD using Landsat images, whose long revisit period (16 days nominally), however, largely limits its applications related to urban air pollution research. To achieve both high spatial resolution and expected revisit period from satellite observation, in this study, a comprehensive AOD retrieval framework is developed for Wide-Field-of-View (WFV) satellite sensors to yield a daily AOD dataset over urban areas with 160 m spatial resolution, based on the Gaofen-1 and Gaofen-6 synergistic observations. To address the crucial challenge that the high spatial resolution and complex urban landscape both contribute a dramatic variation of land surface bidirectional reflectance, a Simulated-Annealing-coupled Semiempirical Modified Rahman-Pinty-Verstraete (SAS-MRPV) scheme is proposed to model and estimate the land surface reflectance (LSR) in the AOD retrieval framework, where the SAS-MRPV scheme is implemented using simulated annealing iteration initialized by the bidirectional reflectance distribution function (BRDF) products from the Moderate Resolution Imaging Spectrometer (MODIS) as a priori knowledge. The validation results demonstrate that the Gaofen WFV AOD retrievals exhibit good agreement with the ground-based AErosol RObotic NETwork (AERONET) and SONET (Sun-sky radiometer Observation NETwork) AOD, demonstrating the correlation coefficient and the expected error (EE)$\pm(0.05 + 0.15\mathrm{AOD}_{\mathrm{AERONET/SONET}})$ ratio respectively reaching up to 0.97 and over 80 %, and only slight bias fluctuations are found under different land cover types, aerosol loading, and seasonal conditions. Moreover, the validation results of Gaofen WFV AOD retrievals, with LSR estimated based on the SAS-MRPV scheme, the MODIS BRDF Products, and the Minimum Reflectance Technique (MRT) method, demonstrate better accuracy and completeness of AOD retrievals using the SAS-MPRV scheme over both natural and impervious land surfaces, indicating the stability and reliability of proposed SAS-MRPV LSR determination

* Corresponding author.
E-mail address: zhangth@ucla.edu (T. Zhang).

https://doi.org/10.1016/j.isprsjprs.2024.04.020
Received 7 October 2023; Received in revised form 25 March 2024; Accepted 19 April 2024
Available online 22 April 2024

scheme in WFV AOD retrieval. In addition to that, the error analyses and quality control results demonstrate that the SAS-MRPV scheme is effective and necessary to guarantee the reliability and accuracy of land surface bidirectional reflectance estimation by identifying and excluding the land surface pixels unsuitable for LSR modeling, which mitigates the uncertainty and yield better accuracy in the final WFV AOD products. Furthermore, the inter-comparison between WFV-derived AOD against the operational MODIS Deep Blue (10 km), Dark Target (3 km), and Multi-Angle Implementation of Atmospheric Correction (MAIAC, 1 km) AOD products demonstrates that the 160 m WFV AOD retrievals, on the basis of obtaining similar aerosol overall descriptions as MODIS AOD retrievals, possess the capability to characterize the spatial distribution of atmospheric pollution at a finer scale with smoother variation under both clean and polluted conditions. With outstanding accuracy and reliable performance, the developed comprehensive high-resolution AOD retrieval framework exhibits substantial potential for operational AOD retrieval of Gaofen WFV satellite observations, which could be directly applied to other urban areas supporting further studies related to air pollution emission management and health risk assessment at extra-fine spatial scale.

1. Introduction

Atmospheric aerosols, comprising solid and liquid suspended particles generated from a variety of natural and anthropogenic origins, play significant roles in climate change and ecosystem (Anderson et al., 2005; Kaufman et al., 2002; Ramanathan et al., 2001; Zhao et al., 2019). Aerosol particles adversely affect air quality and increase the health risks associated with a variety of diseases, thereby influencing morbidity and mortality (Bendixen et al., 2016; Samet et al., 2000; Zhang et al., 2010). The satellite-derived aerosol optical depth (AOD), signifying the integrated aerosol extinction coefficient across the vertical atmospheric column, is widely adopted as a proxy to monitor the spatial distribution and characterize the dynamic variations of atmospheric pollution, benefiting from its advantage on large-scale spatially continuous observation (Hsu et al., 2019; Kaufman et al., 2002).

Satellite remote sensing was initially deployed to retrieve AOD over oceanic regions using the visible and near-infrared spectral bands based on the Advanced Very High Resolution Radiometer (AVHRR) in the late 1970 s (Holben et al., 1992; Holben et al., 1998). Over subsequent decades, satellite-derived AOD was retrieved over both land and ocean using a series of satellite sensors, such as the Moderate Resolution Imaging Spectroradiometer (MODIS) (Levy et al., 2010; Lyapustin et al., 2018; van Donkelaar et al., 2010), Sea-viewing Wide Field-of-view Sensor (SeaWiFS) (Boys et al., 2014; Hsu et al., 2012), the Visible Infrared Imaging Radiometer Suite (VIIRS) (Hsu et al., 2019; Sayer et al., 2019; Wu et al., 2016), the Multiangle Imaging SpectroRadiometer (MISR) (Fan et al., 2023; Gui et al., 2021; Witek et al., 2019), and the Advanced Baseline/Himawari Imagers (ABI/AHI) (Ge et al., 2019; Su et al., 2021; Zhang et al., 2021). The traditional satellite-retrieved AOD products, typically with spatial resolutions ranging from several kilometers to dozens of kilometers, are mostly adopted to support studies related to aerosol radiation effects and climate impacts at global scales (El-Metwally et al., 2011; Kinne et al., 2013). The spatial resolution of satellite-derived AOD products was then improved by implementing advanced or modified aerosol retrieval algorithms to enhance their efficiency and performance in evaluating the environmental effects or health risks of aerosol at regional scales and even city level, such as the operational MODIS 1 km AOD product via the Multi-Angle Implementation of Atmospheric Correction (MAIAC) algorithm (Lyapustin et al., 2011; van Donkelaar et al., 2010), the operational VIIRS 750 m AOD intermediate product without pixel aggregation (Hsu et al., 2019; Levy et al., 2015; Sayer et al., 2019), and the MODIS 500 m AOD datasets via Minimum Reflectance Technique (MRT) algorithm (Wong et al., 2010; Wong et al., 2009; Wong et al., 2011) or Simplified Aerosol Retrieval Algorithm (SARA) (Bilal and Nichol, 2015; Bilal et al., 2013).

With economic development along with dense industrialization and urbanization, developing countries like India and China have been suffering from severe atmospheric pollution issues (Lelieveld et al., 2015). An urgent need arises for monitoring finer aerosols (<500 m) over urban areas, where generally possess high population density and complex landscapes, for supporting delicate urban air pollution studies such as locating precise emission sources (Kumar et al., 2018; Nguyen and Wooster, 2020), community-level health risk assessments (Cai et al., 2021; Kim et al., 2019; Wang et al., 2013) and urban climatology relevance analysis (Boiyo et al., 2018; Carabali et al., 2017; Zhao et al., 2021). Accordingly, high-resolution satellite sensors, such as the Landsat-series (Gillingham et al., 2012; Li et al., 2019; Omari et al., 2019; Sun et al., 2016; Tian et al., 2018; Wei et al., 2017b), Gaofen-1 (Sun et al., 2017; Wu et al., 2019; Yang et al., 2021; Zhang et al., 2018a), HJ-1 (Li et al., 2012; Sun et al., 2010; Zhang et al., 2014), and Sentinel-2 (Lin et al., 2021; Yang et al., 2022b), have been used to retrieve AOD at the city scale with higher spatial resolution from 300 m to even 10 m. However, classic high-resolution satellite sensors are not originally and typically designed for atmosphere observations, thus their revisiting period, which usually ranges from 4-16 days (Guo et al., 2013; Lin et al., 2021), is far from enough for monitoring the aerosol variation information. For instance, the Landsat-8 could hardly obtain one valid AOD map over a specific city in a month due to the possible cloud obscuration, which dramatically limits its significance and value in related research on urban atmospheric pollution.

With the launch of the Gaofen-6 satellite in 2018, which is united with the Gaofen-1 satellite, the synergistic observations from Wide-Field-of-View (WFV) imagers onboard these two satellites possess an overall scanning swath over 1600 km (Dong et al., 2021; Wang et al., 2019b). It provides the feasibility to achieve a revisiting period within two days near the equator and approximately one day at mid to high latitudes, while obtaining 16 m spatial resolution observations, which offers a possibility to retrieve satellite-derived AOD products with both high spatial resolution and ideal revisit cycles. Nevertheless, retrievals of high spatial resolution AOD derived from Gaofen-1 and Gaofen-6 synergistic observations over urban areas are still facing a series of challenges and difficulties. First of all, the WFV imagers onboard Gaofen-1 and Gaofen-6 possess spectral bands only from blue band to near infrared band, where the classic AOD retrieval algorithms, such as Dark Target (DT), Deep Blue (DB) (Levy et al., 2013; Sayer et al., 2014) and their optimized ramification (Sorek-Hamer et al., 2015; Wei et al., 2019), cannot be applied to WFV due to lack of necessary short-wave infrared and deep blue bands. Moreover, how to accurately characterize the land surface reflectance (LSR) over urban areas is also a critical issue, since the anisotropy of bidirectional surface reflectance generally becomes more dramatic along with the increase of spatial resolution and surface type complexity (Roman et al., 2011; Yang et al., 2022a). It has been proven that the uncertainty in estimating LSR can be magnified up to ten times in subsequent AOD retrievals (He et al., 2018; Lin et al., 2022; Roy et al., 2016). However, most previous AOD retrieval algorithms for high spatial resolution satellite sensors have directly applied bidirectional reflectance distribution function (BRDF) models without applicability or accuracy evaluation, or even neglected the land surface heterogeneity assuming the urban land surface as Lambertian surface. Besides, it has been indicated that the geometric calibration error of WFV sensors could reach up to several pixels (Xu et al., 2018; Zhang et al., 2017), while the radiation calibration bias of WFV sensors

also needs solutions attributable to the absence of on-board radiometric calibration system as Landsat series (Feng et al., 2016; Yang et al., 2015). Furthermore, the discrepancies from the spectral response are ubiquitous between sensors due to inevitable differences during sensor manufacturing, which is non-ignorable among WFV sensors onboard Gaofen-1/6 satellites to guarantee radiative responding reliability and consistency (Feng et al., 2016; Yang et al., 2020).

The primary aim of this research is to propose a comprehensive and operational framework for daily high-resolution (160 m) AOD retrievals over urban areas based on Gaofen-1 and Gaofen-6 synergistic observations. The constructed AOD retrieval framework consists of a series of algorithms beginning with WFV-derived Digital Number (DN) values, which include but are not limited to the following primary aspects. The precise geometric correction and radiometric cross-calibration are conducted to ensure the geometric accuracy and radiometric consistency of all WFV sensors during the pre-processing, and the radiometric cross-calibration is using Landsat-8 Operational Land Imager as a reference sensor which has a similar spectrum design and operational orbit with WFV sensors. Moreover, a novel Simulated-Annealing-coupled Semi-empirical Modified Rahman-Pinty-Verstraete (SAS-MRPV) scheme is developed to characterize the land surface bidirectional reflectance over complex urban areas, combined with the performance evaluation of BRDF models over different types of land cover. The particular monthly aerosol models are established by long-term optical properties observations from in-situ AErosol RObotic NETwork (AERONET) sites. And 10×10 original 16 m resolution WFV image pixels are aggregated into one 160 m resolution grid to improve the AOD retrieval accuracy and data reliability, similar as MODIS official AOD algorithm. Furthermore, the WFV-derived AOD dataset is validated against ground-based AERONET and SONET (Sun-sky radiometer Observation NETwork) AOD observations, with sufficient validation of accuracy and reliability using different LSR determination schemes and under different conditions of seasons, land surface types, and aerosol loadings. Then the performances and unique advantages of 160 m Gaofen WFV AOD are illustrated by comparing with MODIS operational DB (10 km), DT (3 km), and MAIAC (1 km) AOD products, as well as their application potential in describing fine spatially resolved aerosol variations over distinct urban landscapes. In addition to that, the error analyses and quality control of the SAS-MRPV scheme in characterizing the LSR are further analyzed and discussed to demonstrate the performance and effectiveness of evaluation metrics adopted in LSR determination.

2. Study area and datasets

2.1. Study area

The experimental area focuses on a typical mega city Beijing (39.3° − 41.1°N, 115.3° − 117.6°E), which is selected as a representative urban area with complex surfaces consisting of various land use types (Wei et al., 2017a). Beijing is the political and cultural center of China (Hao et al., 2020b; Wang, 2013). Given the dense industrialization and urbanization in recent decades (Jin et al., 2022; Shi and Cao, 2020), as well as inter-regional transports of atmospheric pollution (Bilal et al., 2017), atmospheric pollution has become a serious environmental issue that requires prompt solutions and urgent actions in Beijing (Hu et al., 2020; Wang et al., 2022; Xiao et al., 2021). Fig. 1 shows the land cover type and the Digital Elevation Model (DEM) (Du et al., 2016; Feng et al., 2019) of Beijing. The DEM map in Fig. 1a shows that the topography of Beijing is characterized by mountains located in northern and western Beijing, which affects the distribution of meteorological conditions to a certain extent. It was found that this typical topography characteristic of Beijing partially contributes to the frequent haze weather, and such topography tends to block and redirect airflow, leading to the accumulation of air pollution difficult to diffuse (Meng et al., 2019; Wu et al., 2011; Zhang et al., 2018c). Fig. 1b shows the overall land surface types in Beijing, and the locations of four AERONET and SONET sites adopted in this study, where the Beijing SONET and AERONET sites and Beijing-CAMS AERONET site are situated in the heart of urban regions, whereas the XiangHe AERONET site is positioned in the suburban area. The majority of the impervious surfaces in Beijing are most concentrated in the city center, with the rest of the city mostly covered with vegetation, especially in the north and west, and water bodies scattered in the northeast of the city.

2.2. Dataset

2.2.1. Gaofen-1/6 WFV data

In this study, Gaofen-1 and Gaofen-6 WFV Level-0 data is obtained from China Center for Resource Satellite Data and Applications (CRESDA, accessible at https://www.cresda.com). The Gaofen-1 satellite was deployed into orbit on April 26, 2013 (Yang et al., 2021; Zhang and Chen, 2016), and the Gaofen-6 satellite was deployed into orbit on June 2, 2018. Their descending orbits both cross the equator at around 10:30 a.m. Each satellite possesses a band spectrum ranging from 0.45 to 0.89 μm, primarily including the visible and near-infrared bands (Mou et al., 2021; Sun et al., 2021). As illustrated in Fig. 2, both Gaofen-1 and Gaofen-6 operate in polar orbits, where the combination of four single imagers is adopted onboard the Gaofen-1 (Fig. 2b) and the integrated

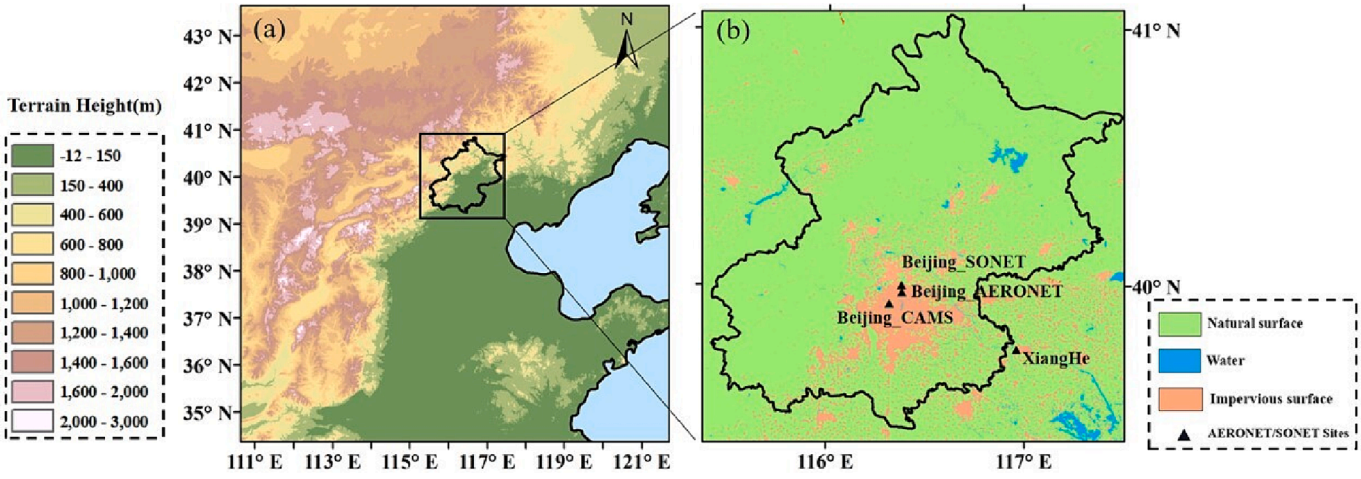

Fig. 1. The terrain characteristics (a) and land cover types (b) of study areas, with the locations of four AERONET/SONET sites represented by black triangles.

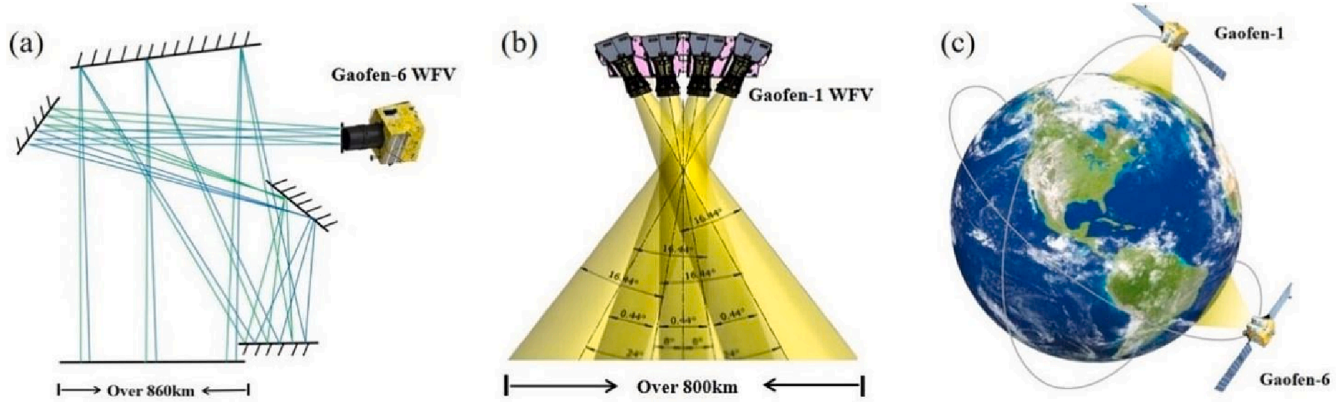

Fig. 2. Schematics of the Wide-Field-of-View (WFV) cameras onboard the Gaofen-1 (b) and Gaofen-6 (a), as well as their synergistic observations (c).

four-mirror off-axis optical system is utilized onboard the Gaofen-6 (Fig. 2a) (Wang et al., 2019a; Wang et al., 2019b), offering a spatial resolution of 16 m, with a temporal resolution ranging between 2 to 4 days due to their scanning swath width over 800 km (Shang and Shen, 2016; Zhang et al., 2017). Gaofen-6 operates collaboratively in a satellite network alongside Gaofen-1 (Fig. 2), which can achieve a nearly daily revisit intervals while preserving high spatial resolution, and the overall scanning swath is over 1600 km from WFV imagers onboard these two satellites. The synergistic observations can achieve a 16 m spatial resolution with a revisit period of two days close to the equator and one day in mid to high latitudinal regions. This research collects all Gaofen-1/6 WFV data from 2013 to 2020 over Beijing, maintaining a cloud cover below 80 %.

2.2.2. *MODIS products*

Three types of MODIS products are adopted in this study: MODIS aerosol products for AOD retrievals, MODIS snow cover data for obtaining snow and ice masks, and MODIS bidirectional reflectance distribution function and albedo (BRDF/Albedo) model datasets for obtaining prior BRDF information in land surface bidirectional reflectance estimation. Only Terra MODIS-derived products are adopted in this study, as the Gaofen-1/6 satellites are equipped with a sun synchronous orbit that intersects the equator at a similar time (10:30 a.m. local time) as Terra.

The aerosol products from MODIS employed for this research include the DB AOD products at 10 km spatial resolution, the DT AOD products at 3 km spatial resolution, and the MAIAC AOD products at 1 km spatial resolution. All the data is with the best quality assurance (QA) flag to ensure its accuracy and reliability. They are used for comparison against the Gaofen WFV AOD retrieval for performance evaluations in different atmospheric pollution conditions. The DB AOD is also used to select clear-sky (Zhang et al., 2022) days in electing candidate images for bidirectional reflectance library constructions, due to its higher spatial coverage compared with the other two. The MODIS C6.1 Level 2 aerosol datasets are obtained from the National Aeronautics and Space Administration (NASA) Level 1 and Atmosphere Archive and Distribution System (LAADS, accessible at https://ladsweb.nascom.nasa.gov/).

The MODIS snow cover dataset used in this research is obtained from the MODIS C6.1 Level 3 daily snow datasets at a spatial resolution of 500 m. Snow products with the best QA flag are obtained from the National Snow & Ice Data Center (NSIDC, accessible at https://nsidc.org/data/mod10a1/). It is employed to obtain snow and ice masks and thus exclude surface areas covered by snow and ice before retrieval.

The MODIS BRDF products (MCD43A1) are collected and introduced as a priori knowledge to improve the fitting accuracy and solving efficiency in LSR determination in this study. Moreover, as a comparison against the proposed SAS-MRPV scheme, the MODIS BRDF products are also applied as land surface reflectance to directly retrieve WFV AOD. The MODIS BRDF products provide the weighting parameters pertinent to the RossThick-LiSparse-Reciprocal (RTLSR) BRDF model, which can characterize pixel-specific anisotropy. The MCD43A1 dataset is disseminated on an 8-day cycle, encompassing 16 days of data collection, and has spatial resolution at 500 m. Data spanning 2013 to 2020 with the good QA flag from MODIS C6.1 is downloaded from NASA LAADS (https://ladsweb.nascom.nasa.gov/).

2.2.3. *AERONET ground-based measurements*

Three ground-based AERONET sites (https://aeronet.gsfc.nasa.gov/) in Beijing are selected in this study. Fig. 1b shows that two of these sites, namely Beijing (39.977°N, 116.381°E) and Beijing_CAMS (39.933°N, 116.317°E), are situated in the urban core, while the site of XiangHe (39.754°N, 116.962°E) is positioned in the suburban regions (Bilal et al., 2019; Bilal et al., 2014; Bilal et al., 2022; She et al., 2017). AERONET Version 3 delivers both optical and physical attributes of aerosols, encompassing spectral AOD, single scattering albedo (SSA), asymmetry factor (g), the complex part of the refractive index (CRI), phase function, and aerosol size distribution (Eck et al., 2019; Lee et al., 2021). These are presented across three distinct data quality, including level 1.0, level 1.5 and level 2.0.

This study employs AERONET data in two aspects. For AOD retrieval validation, V3.0 level 1.5 and level 2.0 measurements from 2013 to 2020 are collected. Given that AOD measurements at 550 nm are not provided by AERONET, the AOD value at this wavelength is interpolated using the Ångström exponent algorithm, utilizing the closest available pair of wavelengths at 675 nm and 440 nm relative to the observed AOD values (Tian et al., 2018). For aerosol type assumption, the V3.0 level 2.0 measurements from 2013 to 2020 are collected in this study. Aerosol optical properties encompassing single scattering albedo, asymmetry parameter, size distribution, and the complex index of refraction, are adopted for the determination of long-term customized monthly aerosol models in Beijing, which would be more accurate than the seasonal aerosol type assumption (Wei et al., 2019).

2.2.4. *SONET ground-based measurements*

The SONET (http://www.sonet.ac.cn/en/index.php) is a network of observation sites established by the Chinese Academy of Sciences (CAS) and related organizations in a representative region of China. The CE318-DP used within the SONET network is equipped with radiance and polarization measurements across eight wavelengths from 340 to 1640 nm, which can provide long-term and continuous observation at approximately 15-minute intervals. This enables the capture of aerosol optical, physical, and chemical composition parameters throughout the atmosphere (Ma et al., 2016; Shi et al., 2022). In this study, the Beijing SONET site (116.4°E, 40.0°N) is included to validate the WFV AOD retrieval results through its combination with AERONET AOD data. As illustrated in Fig. 1b, the Beijing SONET site is situated in the impervious

surface area. This study employs SONET level 1.5 measurements gathered from 2013 to 2020 for AOD retrieval validation. Given that AOD measurements at 550 nm are not provided by SONET, the AOD value at this wavelength is interpolated using the Ångström exponent algorithm, utilizing the closest available pair of wavelengths at 440 nm and 675 nm relative to the observed AOD values (Shi et al., 2022).

2.2.5. ECMWF reanalysis datasets

The ozone and water vapor data employed in this research are obtained from the European Centre for Medium-Range Weather Forecasts (ECMWF) (Liu et al., 2015; Pan et al., 2011), and the ERA5 Reanalysis Data (0.25 × 0.25°) (Hersbach et al., 2020; Urban et al., 2021). ERA5 is the fifth-generation ECMWF reanalysis and provides an extended temporal sequence of atmospheric fields featuring both high spatial and temporal resolution. The monthly total column water vapor data and monthly ozone total columns gridded data for 2013–2020 are downloaded from ECMWF (https://www.ecmwf.int/), and applied to express the gas absorption and Rayleigh scattering terms during the pre-processing and retrieval processes in this study.

2.2.6. Global land cover data

Land cover information is derived from the Finer Resolution Observation and Monitoring of Global Land Cover (FROM-GLC10, accessible at https://data-starcloud.pcl.ac.cn/zh/resource/1) (Gong et al., 2019), and it is used for land use classification, pixel selection and land-type changes detection in this study. The adopted dataset encompasses ten distinct land cover classifications: Cropland, Forest, Grass land, Shrubland, Wetland, Water, Tundra, Impervious surface, Bare-land and Snow/Ice. These classifications are delineated at a spatial granularity of 30 × 30 m. Meanwhile, the dataset is also utilized to distinguish the impervious land surfaces from the natural land surfaces, and applied to evaluate the performances of WFV AOD retrievals under different urban land surface type conditions.

2.2.7. Landsat 8 OLI data

Surface reflectance products from the Landsat 8 Operational Land Imager (OLI) are obtained from the United States Geological Survey (USGS, accessible at https://www.usgs.gov/land-resources/), and the quality assessment band of Landsat-8 OLI image (https://landsat.usgs.gov/qualityband) is employed to eliminate cloud and snow pixels to ensure the data validity. Analogous spectral ranges and overpass times facilitate the feasibility of cross-calibration for the WFV sensor, with the OLI serving as the reference instrument (Chen et al. 2017; Feng et al., 2016). Landsat 8 OLI data is used to ensure the radiance reliability of all WFV sensors in this research, where the image pairs from Gaofen-1/6 WFV and Landsat-8 OLI between 2013 and 2020 in Dunhuang calibration ground with minimal cloud coverage on the same day are selected.

2.2.8. Road network and emission unit data

In this study, the road density and the emission units serve as indicators of vehicle-generated and industrial atmospheric pollution, respectively, representing the two major intra-city atmospheric pollution emission sources. Road network data from OpenStreetMap (Lautenschlager et al., 2020) was extracted for the analysis of vehicle-related atmospheric pollution. For the analysis of intra-city industrial influence on atmospheric pollution, key emission units including a variety of industrial zones and factories associated with intensive atmospheric pollution emission were identified using data from the 2019 report published by the Beijing Municipal Ecology and Environment Bureau (Dong et al., 2023a).

3. Methodology

Assuming a plane-parallel atmosphere and a non-Lambertian ground surface, the top-of-atmosphere (TOA) satellite-based spectral reflectance $\rho_{TOA}(\theta_s, \theta_v, \varphi_s, \varphi_v)$ could be formulated as follows (Vermote et al., 1997).

$$\rho_{TOA}(\theta_s, \theta_v, \varphi_s, \ \varphi_v) = T_g\left[\rho_{atm}(\theta_s, \theta_v, \ \varphi_{|s-v|}) + \frac{T^{\downarrow}(\theta_s)\cdot T^{\uparrow}(\theta_v)\cdot\rho_s(\theta_s, \theta_v, \varphi_s, \varphi_v)}{1-\rho_s(\theta_s, \ \theta_v, \varphi_s, \varphi_v)\cdot S}\right] \quad (1)$$

where θ_s is the solar zenith angle and θ_v is the satellite zenith angle; φ_s represents the solar azimuth angle and φ_v refers to the satellite azimuth angle; $\varphi_{|s-v|}$ denotes the angular difference in azimuth between the Sun and the satellite; T_g is the total gaseous transmittance; $\rho_{atm}(\theta_s, \theta_v, \varphi_{|s-v|})$ refers to the reflectance of the atmosphere path directly emanating from atmospheric molecules and aerosols; $T\downarrow(\theta_s)$ refers to downward atmospheric transmittance pertaining to solar orientation, and $T\uparrow(\theta_v)$ represents the upward atmospheric transmittance corresponding to sensor-viewing orientation; $\rho_s(\theta_s, \theta_v, \varphi_s, \varphi_v)$ signifies the land bidirectional spectral reflectance, while S represents the atmospheric hemisphere albedo.

It is well known that the key of AOD retrieval is the atmosphere-surface decoupling, primarily including the atmosphere intrinsic contribution and atmosphere-surface coupled contribution. One of the crucial components for high spatial resolution AOD retrieval, namely land surface bidirectional reflectance estimation, is elaborated upon extensively in section 3.2. The parameters for the atmosphere intrinsic contribution can be computed using the Second Simulation of the Satellite Signal in the Solar Spectrum Vector (6SV) radiation transmission model under given geometric conditions. This can be accomplished by inputting the atmospheric model and aerosol loading, based on assumptions regarding the aerosol model. The comprehensive Gaofen WFV AOD retrieval framework illustrated in Fig. 3 consists of several aspects regarding pre-processing, the SAS-MRPV scheme for LSR determination, aerosol model assumption, the 6SV model for AOD retrieval, and data validation and evaluation. These aspects are expounded upon in detail in the subsequent sections.

3.1. Key procedures in pre-processing of Gaofen WFV data

3.1.1. Pixel selection strategy

Gaofen WFV AOD retrieval is conducted under strict cloud-free land surface conditions. Prior to commencing the AOD retrieval procedures, it is essential to exclude pixels that do not meet the specified criteria. These criteria encompass surface pixels containing cloud, cloud shadow, water bodies, shore, snow/ice and variation of land use types. Precisely identifying clouds and cloud shadows within Gaofen-1/6 WFV imagery presents a notable challenge, largely stemming from the constraints imposed by the limited spectral bands. In this study, the automated methodology amalgamating multiple features, termed as the Multi-Feature Combined (MFC) approach, tailored for the discernment of clouds and their associated shadows within WFV imagery is adopted based on our prior research (Li et al., 2017), and the WFV cloud and cloud shadow detection process attains a high average overall accuracy of 96.8 %. In addition, the water mask is derived from global land cover data, and the shore mask is generated through a morphological buffering operation extending 10 pixels from the corresponding water mask. The snow/ice surface mask is delineated when the snow/ice cover percentage, as indicated by the MODIS snow/ice dataset, deviates from an exact value of 0 %. Besides, periodic and permanent changes in surface type are excluded to ensure the reliability of land surface BRDF modeling. The land use change mask is established through an evaluation of transitions between natural surfaces and impervious surfaces, either from the former to the latter or vice versa, throughout the entire experimental duration (Zhang et al., 2022). Furthermore, to mitigate the significant errors stemming from the assumption of a spherical atmosphere as a plane-parallel atmosphere under extreme angular conditions, pixels characterized by a solar zenith angle or satellite azimuth exceeding 72° are excluded from consideration.

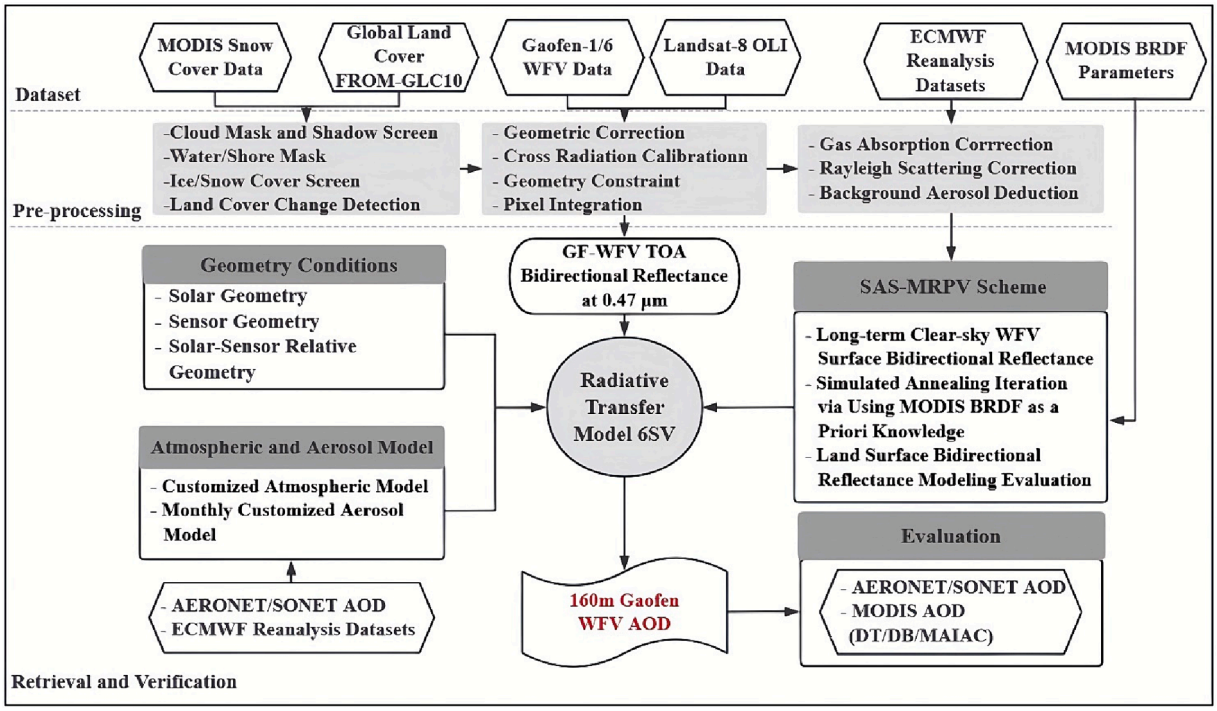

Fig. 3. Schematics of Gaofen WFV AOD retrieval framework.

3.1.2. Cross-radiation calibration

Given that the Gaofen-1/6 satellites lack onboard calibrators, vicarious calibration and cross-calibration procedures are widely employed for on-orbit calibration. In general, vicarious calibration presents challenges due to its labor-intensive nature, significant costs, and limited spatial coverage. In order to address these constraints, a cross-calibration methodology has been introduced, utilizing the imagery from a rigorously calibrated satellite sensor as a reference (Feng et al., 2016). In this study, a radiometric cross-calibration based on our previous research (Dong et al., 2023b) is developed for Gaofen-1 and Gaofen-6 WFV based on Landsat-8 OLI images. This calibration process can ensure the reliability and consistency of radiance measurements across all WFV imagers onboard Gaofen-1 and Gaofen-6, with a calibration uncertainty less than 8 %.

3.1.3. Auto-geometric correction

The accuracy of geometric correction plays a critical role in the AOD retrieval, especially when constructing the land surface BRDF models. The auto-calibration method for WFV sensors that utilizes flat terrain to detect nonlinear distortions is adopted in this study based on our previous study (Zhang et al., 2017), where the orientation accuracy could be controlled within 0.6 pixel evaluated by ground control field checkpoints with the residual errors manifested as random errors.

3.1.4. Pixel integration

Prior to the pre-processing of WFV image data, data integration was undertaken to guarantee spatial coherence across various data types. Every auxiliary dataset, encompassing both the products derived from MODIS and reanalysis data, was initially reprojected to the World Geodetic System 1984 (WGS-84) geographic coordinate system. Subsequently, they underwent resampling through bi-linear interpolation to align with the Gaofen WFV geographic grids, which have a spatial resolution of 16 m. In addition, analogous to the operational AOD retrieval algorithm employed by MODIS, where pixel integration has been adopted to obtain aerosol information with less uncertainty (Zheng et al., 2021). This method involves the downward aggregation of AOD retrieval results from 500 m into 1 km, 3 km, and 10 km (Levy et al., 2013; Lyapustin et al., 2018; Sayer et al., 2014). Similarly, the procedure of downward aggregation is applied to the Gaofen WFV retrieval results, initiating from a spatial resolution of 16 m to a coarser resolution of 160 m, with 10 × 10 pixels aggregated by screening the maximum and minimum 30 % and averaging the median 40 %.

3.2. Land surface reflectance (LSR) determination

3.2.1. Significance of characterizing land surface bidirectional reflectance in WFV AOD retrieval

The essence of satellite-based aerosol retrieval from TOA reflectance is to disentangle the atmospheric and surface reflectance contributions. Therefore, an appropriate surface estimation scheme is crucial for ensuring the reliability and accuracy of urban AOD retrievals, since the urban areas have complex landscapes with relatively high surface reflectance (Zhang et al., 2022). In addition, the spatial resolution of the Gaofen WFV is only 16 m and the observation angle varies considerably, which will lead to a dramatic change in surface reflectance over the urban surface (Wang et al., 2018). MODIS, Polarization and Directionality of Earth Reflectance (POLDER) and Multi-angle Imaging Spectroradiometer (MISR) are three currently available sensors able to provide land surface bidirectional reflectance with distinct sun-sensor geometry conditions (Zheng et al., 2020). However, the resolutions of these existing BRDF data or products are too coarse to be directly applied for WFV AOD retrieval, as well as the distinct spectral response functions between different sensors. Therefore, it is of significance and necessity to characterize the WFV-specific land surface bidirectional reflectance over complex urban areas.

3.2.2. Selection of core BRDF model for LSR determination scheme

There are several BRDF models widely used to characterize the land surface bidirectional reflectance in the current satellite algorithms, such as the modified Rahman-Pinty-Verstraete (MRPV) model (Engelsen et al., 1997,1998; Rahman et al., 1993a; Rahman et al., 1993b; Solheim et al., 2000), which is the operational BRDF model in MISR BRDF/Albedo algorithm (Armston et al., 2007), and the kennel-driven semi-empirical BRDF model RossThick-LiSparse-Reciprocal (RTLSR), which is

known as the official algorithm for characterizing bidirectional reflectance anisotropies of the land surface in MODIS (Wanner et al., 1997). In this study, two operational BRDF models above, namely the RTLSR BRDF model and the MRPV model, are both adopted for characterizing the land surface bidirectional reflectance for WFV sensors over urban areas, to select the core BRDF model in the LSR determination scheme with better performances, combined with the applicability evaluation of both BRDF models over various land cover types. For reasonable and quantitative comparison, the model sensitivity analyses are carried out by applying the RTLSR and the MRPV BRDF models for fitting the exactly same WFV land surface bidirectional reflectance datasets with distinct sun-sensor geometry conditions across diverse land cover types situated within the study regions. The experiments and results are described in Supplementary Materials Text S1 and Table S1, which show that the model fitting accuracy of the MRPV model is generally comparable to those of the RTLSR model over natural land surfaces, while the MRPV model performs better in fitting the observed WFV reflectance over most impervious land surfaces, where the MRPV-derived fitting accuracy achieves the RMSE less than 0.04 and R greater than 0.86 under most situations. The probable reason is that the MRPV model performs better when considering the large angle observation and describing the backward hotspot effects, which is significant and necessary for urban surface reflectance estimation for WFV sensors. It should be noted that the RTLSR model may encounter mathematical problems when the view zenith angle is large in the comparison experiment, which is resolved by forcing it to be equal to the normal range of boundary values in accordance with prior research (Shuai et al., 2008). In contrast, the MRPV model calculation process has always been smooth, indicating its reliability in estimating bidirectional surface reflectance under relatively large viewing geometry conditions. Therefore, the MRPV model is selected as the core BRDF model in the subsequent SAS-MRPV scheme in this study.

3.2.3. Detailed descriptions for the SAS-MRPV scheme

The original Rahman-Pinty-Verstraete (RPV) model could be expressed as Eqs. (2)-(6) (Pacifici et al., 2014). Considering the solar zenith angle θ_s, the view zenith angle θ_v, and the relative azimuth angle between the view and solar positions φ, the bidirectional reflectance obtained by the RPV model is calculated as follows.

$$\rho_{RPV}(\theta_s,\theta_v,\varphi) = \rho_0 \bullet \frac{cos^{k-1}\theta_s cos^{k-1}\theta_v}{(cos\theta_s + cos\theta_v)^{1-k}} \bullet F(g,\vartheta) \bullet H(G,\rho_0) \quad (2)$$

The RPV model systematically deconstructs the observed angular surface reflectance into three independent components: the representation of amplitude ρ_0, the shape anisotropy k, and the factor of asymmetry ϑ. The parameter $\rho_0 \in [0,1]$ characterizes the intensity of the target, remaining invariant to angular fluctuations. The parameter$k \in [0,2]$ denotes the anisotropy of the target. Anisotropy patterns are delineated by the values of k; values less than 1.0 signify a bowl-shaped pattern, whereas values exceeding 1.0 correspond to a bell-shaped configuration. The ideal case of$k = 0$ represents a Lambertian surface. Conclusively, the asymmetry factor θ, constrained within the range [-1,1], modulates the proportion of forward scattering, $\theta \in (0,1]$ and backward scattering, $\theta \in [-1,0)$ (Pacifici et al., 2014). According to:

$$F(g,\vartheta) = \frac{1-\vartheta^2}{(1+\vartheta^2+2\vartheta cosg)^{3/2}} \quad (3)$$

with

$cosg = cos\theta_s cos\theta_v + sin\theta_s sin\theta_v cos\varphi$ (4) and

$$H(G,\rho_0) = 1 + \frac{1-\rho_0}{1+G} \quad (5)$$

where $H(G,\rho_0)$ in Eq. (2) and Eq. (5) is the term to describe the hotspot, which captures the backward hotspot effects which are significant for urban areas in this study (Pacifici et al., 2014), with

$$G(\theta_S,\ \theta_V,\varphi) = (tan^2\theta_s + \ tan^2\theta_v - 2tan\theta_s tan\theta_v cos\varphi)^{1/2} \quad (6)$$

The Modified RPV model (Engelsen et al., 1998) employs a logarithmic transformation and a least squares solution to streamline the process of obtaining parameters in the RPV model. As part of this modification, the function in Eq. (3) was substituted with the following expression.

$$F(g,b) = exp(b \cdot cosg) \quad (7)$$

where b is the parameter in the MRPV model for describing the BRDF asymmetry. One significant benefit of MRPV models is their ability to effectively simulate the intricate 3-D BRDF field, which is accomplished by utilizing the product of three angular functions in the equations above (Liu et al., 2016).

To enhance the convergence stability and fitting accuracy for the nonlinear MRPV model, a Simulated-Annealing-coupled Semiempirical Modified Rahman-Pinty-Verstraete (SAS-MRPV) scheme is proposed in this study aiming to achieve the global optimization for MRPV BRDF model through using simulated annealing iteration, which is initialized by the MODIS BRDF dataset as a priori knowledge to obviously improve the convergence efficiency and fitting accuracy (Mafarja and Mirjalili, 2017). To be specific, the long-term 16 m WFV land surface bidirectional reflectance datasets were firstly collected, after conducting gas and background aerosol corrections on clear-sky candidate WFV images. Then these WFV land surface bidirectional reflectance datasets with corresponding sun-sensor geometry, including satellite zenith angle, sun zenith angle, and relative azimuth angle, were served as original datasets to fit the MRPV model through the simulated annealing iteration approach. In order to reduce the number of iterations required for model convergence and confine the iteration boundary, the initial land surface bidirectional reflectance for each pixel has been configured and estimated by utilizing the MODIS BRDF products based on the MODIS operational RTLSR BRDF model, where the MODIS BRDF parameters extracted at the center of each Gaofen pixel. Through continuous iteration of the simulated annealing algorithm, the convergence accuracy for the MRPV model representing the WFV land surface bidirectional reflectance datasets was gradually enhanced to achieve the global optimal solution, resulting in the most accurate estimation for the MRPV BRDF model parameters for each WFV pixel.

In addition to that, similar to the quality assessment implemented in MODIS operational algorithms for BRDF/albedo products, two evaluation metrics Root Mean Square Error (RMSE) and Weight of Determination (WoD) (Jiao et al., 2014) are used to assess the accuracy and reliability in characterizing the land surface bidirectional reflectance for WFV, where the RMSE serves as an indicator of deviation in model-fitting, whereas the WoD offers an assessment of retrieval confidence based on the provided angular samplings (Shuai et al., 2008). Furthermore, the combination of these two assessment metrics is employed to conduct the quality control in the SAS-MRPV modeling and the subsequent AOD retrieval processes, which will be discussed in the later error analysis section.

$$RMSE = \sqrt{\frac{1}{n}\sum_{i=1}^{n}(R\_model_i - R\_obs_i)^2} \quad (8)$$

where n represents the number of models fitted and WFV observed bidirectional reflectance pairs. R_obs is the observed surface reflectance, and R_model is the surface reflectance derived from the surface BRDF characteristics through the BRDF model. A higher RMSE value suggests larger deviations in model fitted and WFV observed bidirectional reflectance values.

As for the calculation of WoD, using the theory that originates with Gauss, the uncertainty (error) ε_u expected in u may be expressed as (Lucht and Lewis, 2000):

$$\varepsilon_u = e\sqrt{\frac{1}{w_u}} \tag{9}$$

where e is an estimate of standard error in the observed data, and $1/w_u$ is the weight of determination of term u. In this study, the calculation of WoD is defined as follows.

$$WoD = \frac{\sigma}{RMSE} \tag{10}$$

where σ is the standard error of observed bidirectional reflectance samplings, and RMSE is the root mean squared error of observed bidirectional reflectance samplings.

3.3. Aerosol-Type assumptions

The aerosol type which elucidates both the chemical composition and optical properties within a designated area, stands as a pivotal factor influencing the accuracy of AOD retrieval. Key optical attributes defining the aerosol type encompass SSA, asymmetry factor g, and CRI. SSA quantifies total extinction due to scattering and epitomizes proficiency in electromagnetic radiation absorption and scattering. The factor g delineates the balance between forward and backward scattering and maintains consistent within a specific aerosol type. The CRI sheds light on the particle capacity for light scattering and absorption. Specifically, the real part (RP) of the CRI details the potential of aerosol particles to diminish radiative energy, while its imaginary part (IP) underscores the absorption capacity of aerosol particles. The calculation of aerosol optical properties is conducted using the MIE scattering model within the framework of the 6SV model. The 6SV radiation transmission model (RTM) employs both the refractive index and aerosol size distribution to characterize the aerosol type derived from sun photometer data.

Table 1 presents the aerosol optical properties of monthly aerosol models employed in the AOD retrieval in this study, and it indicates that the SSA attains its peak value in July, while its lowest value is observed in January. The asymmetry factor g illustrates a similar trend, with the largest value occurring in July and the smallest value in November. The RP-CRI and IP-CRI reach their peak values in January and achieve their lowest values during June. All the aerosol optical properties exhibit conspicuous seasonal variation, and it could be observed that there still exist slight changes within each season. Therefore, compared with the seasonal aerosol model, the monthly aerosol model adopted in this study can achieve more accurate aerosol model assumptions, further reducing the accuracy uncertainty in the subsequent AOD retrieval.

3.4. AOD retrieval using the 6SV model

The retrieval of aerosol information from satellite observations can be obtained by comparing the observed reflectance with that computed by the RTM. However, executing the RTM in real-time can be time-consuming. Therefore, the AOD retrieval algorithm for WFV is formulated using streamlined Look-Up Tables (LUT) derived from the 6SV model to improve computational efficiency and avoid running the RTM for every pixel.

Table 2 elucidates the LUT methodology employed for AOD retrieval (Cheng et al., 2012; Jiang et al., 2022; Sun et al., 2017; Zhang et al., 2018b). This approach is predicated on the 6SV model, incorporating tailored atmospheric models, a range of aerosol loadings (AOD), distinct sun-sensor geometric configurations, and varied elevation conditions. By combining the land surface bidirectional reflectance estimated through the SAS-MRPV scheme and the aerosol optical properties contained within the monthly aerosol model, the pre-established LUT enables the calculation of simulated TOA reflectance. The simulated TOA reflectance can then be computed utilizing the constructed LUT under a given geometry and atmospheric conditions. A nonlinear interpolation method between simulated TOA reflectance and TOA reflectance observed by the satellite is utilized to determine the exact AOD value for each pixel.

3.5. Accuracy validation and performance evaluation of AOD retrievals

When the WFV AOD retrieval process is completed, the validation is carried out by comparing the WFV AOD retrieval results with AERONET and SONET AOD and three MODIS AOD products, namely DB, DT, and MAIAC AOD. Statistical accuracy indicators, including the mean absolute error (MAE), mean relative error (MRE), RMSE, relative root mean square error (RRMSE), correlation coefficient (R), and the expected error (EE) envelope defined in Eq. (11) to Eq. (15), are employed to assess the accuracy of WFV AOD retrieval results against AERONET and SONET AOD. Specifically, the mean AOD value is extracted within a 30-minute window around the Gaofen WFV overpass to ensure temporal and spatial alignment. Subsequently, the AOD retrievals for WFV are conducted over a standard sampling grid of 3 × 3 pixels at the AERONET and SONET sites. The mean of the effective values, where AOD exceeds 0, is designated as the AOD retrieval for this site.

$$MAE = \frac{1}{n}\sum_{i=1}^{n}|WFV\_AOD_i - AERONET/SONET\_AOD_i| \tag{11}$$

$$MRE = \frac{1}{n}\sum_{i=1}^{n}\frac{|WFV\_AOD_i - AERONET/SONET\_AOD_i|}{AERONET/SONET\_AOD_i} \tag{12}$$

$$RMSE = \sqrt{\frac{1}{n}\sum_{i=1}^{n}(WFV\_AOD_i - AERONET/SONET\_AOD_i)^2} \tag{13}$$

$$RRMSE = \sqrt{\frac{\frac{1}{n}\sum_{i=1}^{n}(WFV\_AOD_i - AERONET/SONET\_AOD_i)^2}{\sum_{i=1}^{n}(AERONET/SONET\_AOD_i)^2}} \tag{14}$$

Table 1
Monthly aerosol optical properties used in AOD retrieval.

Month	SSA (0.47 m)	g (0.47 μm)	RP-CRI (0.47 μm)	IP-CRI (0.47 μm)
January	0.884	0.679	1.504	0.016
February	0.911	0.679	1.491	0.011
March	0.919	0.682	1.501	0.008
April	0.929	0.682	1.498	0.006
May	0.920	0.676	1.498	0.006
June	0.961	0.709	1.448	0.004
July	0.963	0.717	1.453	0.004
August	0.954	0.711	1.449	0.005
September	0.943	0.703	1.474	0.007
October	0.933	0.699	1.500	0.008
November	0.906	0.656	1.490	0.011
December	0.891	0.692	1.493	0.014

Table 2
The list of input variables used for Gaofen WFV AOD retrieval LUT.

Input Variables	Number of Entries	Entries
Satellite Zenith Angle (°)	13	0, 6, 12, 18, 24, 30, 36, 42, 48, 54, 60, 66, 72
View Zenith Angle (°)	13	0, 6, 12, 18, 24, 30, 36, 42, 48, 54, 60, 66, 72
Relative Azimuth Angle (°)	14	0, 12, 24, 36, 48, 60, 72, 84, 96, 108, 120, 132, 144, 156
AOD at 0.55 μm	9	0, 0.25, 0.5, 0.75, 1, 1.5, 2, 3, 5
Terrain height (km)	2	0, 1
Surface bidirectional reflectance	4	0, 0.1, 0.2, 0.3
Customized water–vapor (cm·atm)	10	0.4, 0.8, 1.2, 1.6, 2.0, 2.4, 2.8, 3.2, 3.6, 4.0
Customized ozone content (cm·atm)	8	0.25, 0.75, 1.25, 1.75, 2.25, 2.75, 3.25, 3.75

$$EE = \pm(15\% \times AERONET/SONET\_AOD + 0.05) \quad (15)$$

where n is the number of WFV-AERONET/SONET AOD pairs. The MAE quantifies the difference between WFV-derived AOD and AERONET/SONET AOD values, while the MRE evaluates the relative error between WFV-derived AOD and AERONET/SONET AOD values. The RMSE represents the dispersion extent within these differences. A higher RMSE value suggests a more significant deviation in WFV-derived AOD values. RRMSE is a root mean square error metric that has been scaled to the actual value and then normalized by the RMSE. While the scale of the original measurements limits RMSE, RRMSE can be used when comparing different measurement techniques. Also, RRMSE expresses the error relatively. The EE represents the fraction of WFV-derived AOD values that match AERONET/SONET AOD values within the expected error.

4. Results and discussion

4.1. Validation against AERONET/SONET AOD measurements

This study validates the performance of the Gaofen WFV AOD retrieval algorithm using AERONET/SONET AOD measurements at 550 nm under different LSR determination schemes and land cover types (Fig. 4), satellite types (Fig. 5), aerosol loadings (Fig. 6), yearly (Fig. 7), and seasonal conditions (Fig. 8), respectively.

The accuracy of WFV AOD retrievals against AERONET and SONET sites were compared, where the LSR was estimated by different LSR determination schemes, including the SAS-MRPV scheme, the MODIS BRDF Products, and the Minimum Reflectance Technique (MRT). The descriptions for WFV LSR determination via MODIS BRDF Products and MRT method are described in Supplementary Materials Text S2. As illustrated in Fig. 4, AOD retrievals through LSR estimated based on both the SAS-MRPV scheme (Fig. 4a) and MODIS BRDF Products (Fig. 4b) can achieve high accuracy over natural (XiangHe AERONET site) and impervious land surfaces (Beijing, Beijing-Camps AERONET sites, and Beijing SONET site), where the values of R and the EE ratio reach up to 0.97 and over 80 %, respectively, with the MAE, MRE and RMSE values less than 0.07, 0.4 and 0.13. However, AOD retrievals through LSR estimated based on the MRT have relatively large uncertainty, as indicated by larger values of evaluation metrics and lower values of the percentage of the matchups falling within the EE envelope. This indicates that the LSR determination scheme which considers the land surface BRDF effect has a prominent advantage in estimating surface impacts on AOD retrievals. Moreover, the accuracy of the WFV AOD

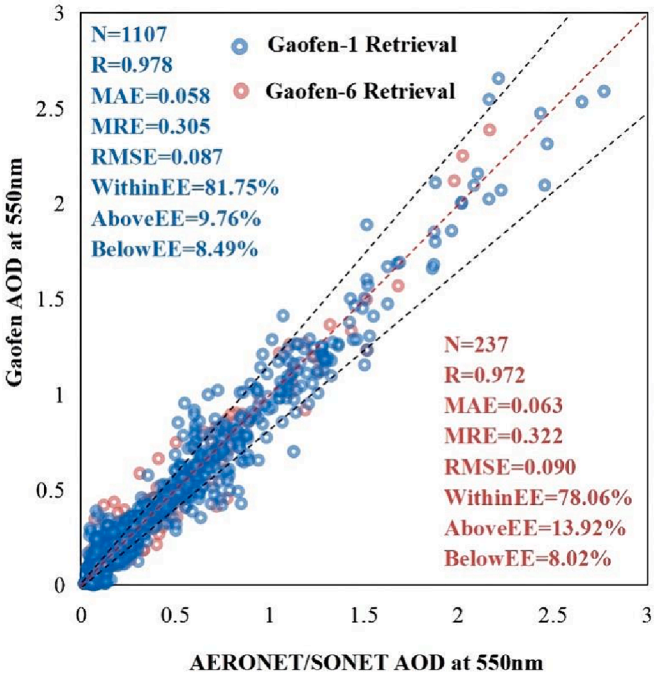

Fig. 5. Validation of the Gaofen WFV AOD retrievals of Gaofen-1 (blue circles) and Gaofen-6 (red circles) against the AERONET/SONET AOD measurements in Beijing from 2013 to 2020. The EE envelope lines are denoted by black dashed lines, while the 1:1 reference line is highlighted in red dashes. (For interpretation of the references to color in this figure legend, the reader is referred to the web version of this article.)

retrieval through LSR estimated based on the SAS-MRPV scheme and MODIS BRDF Products over natural land surfaces exhibits a superiority over that of impervious land surfaces to some extent, with superior evaluation metrics and a larger proportion of matchups falling within the EE envelope. To be specific, the uncertainty of AOD retrieval through LSR estimated based on the MODIS BRDF Products is lower over natural land surfaces compared to impervious land surfaces, while the AOD retrieval through LSR estimated based on the SAS-MRPV scheme exhibits comparable performance across both land surface types, with over 80 % of matchups falling within the EE envelope and RMSE values of less than 0.1 for both natural and impervious land surfaces. This demonstrates the consistent performance of the SAS-MRPV LSR determination

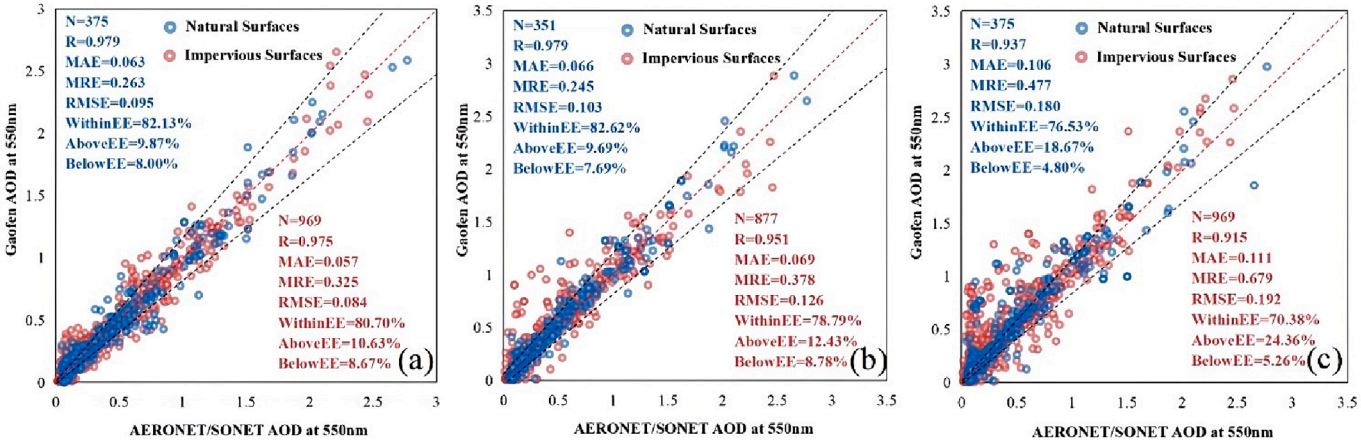

Fig. 4. Validation results of the Gaofen WFV AOD retrievals through LSR estimated based on (a) the SAS-MRPV scheme, (b) the MODIS BRDF Products, and (c) the Minimum Reflectance Technique (MRT), against the AERONET/SONET AOD measurements in Beijing from 2013 to 2020 over natural (blue circles) and impervious (red circles) land surfaces, respectively. The EE envelope lines are denoted by black dashed lines, while the 1:1 reference line is highlighted in red dashes. (For interpretation of the references to color in this figure legend, the reader is referred to the web version of this article.)

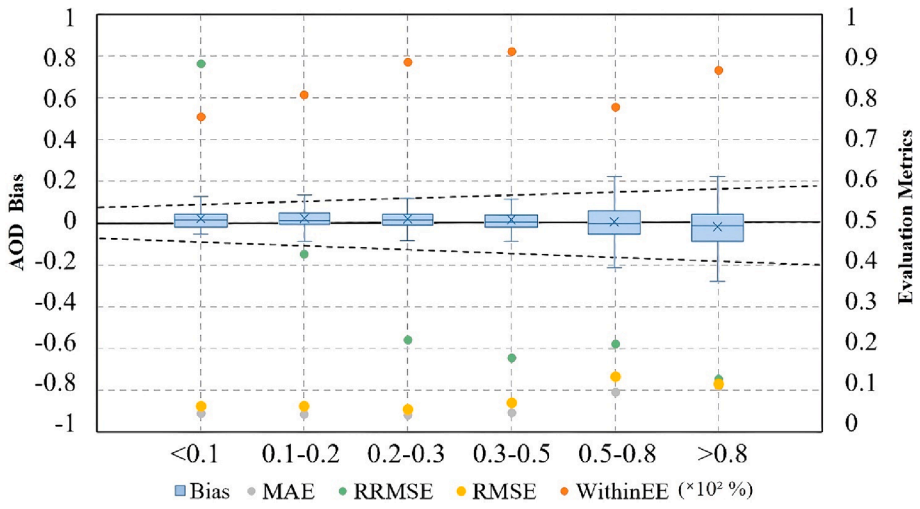

Fig. 6. The AOD bias, RMSE, MAE, and the ratio of matchup pairs falling within the EE envelope for WFV AOD retrievals against AERONET/SONET AOD measurements across varying aerosol loading conditions.

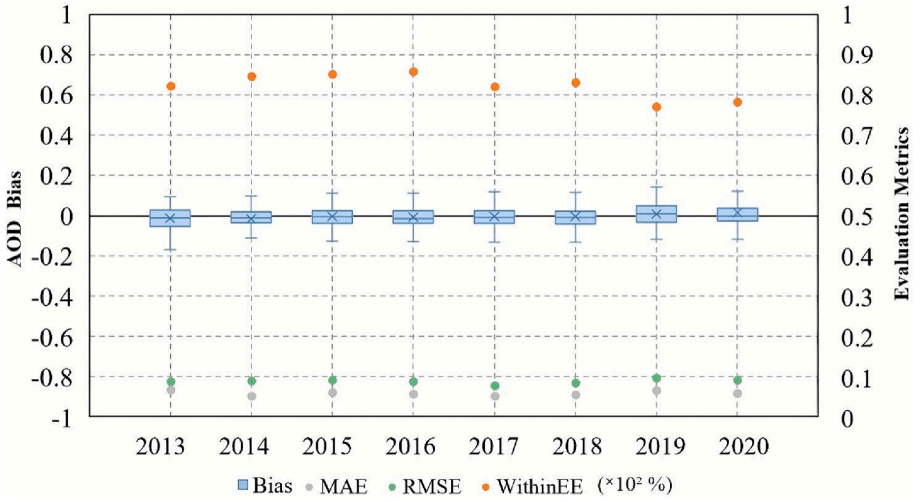

Fig. 7. The AOD bias, MAE, RMSE, and the ratio of matchup pairs falling within the EE envelope for WFV AOD retrievals against AERONET/SONET AOD measurements for each year.

scheme under different land cover types. Furthermore, it can be seen from the proportion falling in the EE lines that there are more deviations in the AOD retrieval through LSR estimated based on the MODIS BRDF Products over impervious areas than based on the SAS-MRPV scheme, possibly due to that the land surface of urban areas is complex, the uncertainty may be introduced when applying relatively coarse spatial resolution of MODIS 500 m to WFV 16 m. Besides, fewer matchups (N) could be found in AOD retrieval through LSR estimated based on the MODIS BRDF Products compared to the N values of AOD retrievals through LSR estimated based on the other two LSR determination schemes, which is probably caused by intrinsic data missing within the MODIS BRDF Products. Furthermore, for the AOD retrieval through LSR estimated based on the MRT, the AOD overestimation is obvious over both natural and impervious land surfaces, where more significant overestimation appears over impervious land surfaces than that over natural land surfaces, which may be due to the BRDF effect in impervious areas is more significant than that over natural areas, and thus the overestimation of AOD values may be more significant in urban areas, which is reflected by larger values of evaluation metrics and lower values of proportion of matchups falling within the EE envelope less than 77 %.

In addition to that, the comparison and analysis of the spatial distribution details of WFV AOD retrievals through LSR estimated based on different methods, which are illustrated and described in Supplementary Materials Figure S1 and Text S3, indicate that AOD retrieval through LSR estimated based on the SAS-MPRV scheme can achieve more complete coverage while exhibiting generally stable performances under both clean and polluted conditions. As contrast, the occurrence of abnormal AOD values retrieved based on MODIS BRDF Products and the MRT method is primarily attributed to applying 500 m MODIS BRDF data to characterize 16 m land surface bidirectional reflectance and typical underestimation of land surface reflectance in MRT, respectively.

To explore the impact of different satellites on the retrieval of AOD based on satellite constellation synergistic observation, Fig. 5 shows the validation of the Gaofen WFV AOD retrievals against the AERONET/SONET AOD for Gaofen-1 and Gaofen-6, respectively. The results show a good correlation between WFV AOD retrievals of both Gaofen-1 and Gaofen-6 and AERONET/SONET AOD, where the values of R and the EE ratio were as high as 0.97 and more than 78 %, respectively. Additionally, the MAE, MRE, and RMSE values of less than 0.06, 0.33, and 0.1, respectively, indicate that the accuracy of the WFV-derived AOD is reliable over both Gaofen-1 and Gaofen-6. Overall, the WFV AOD

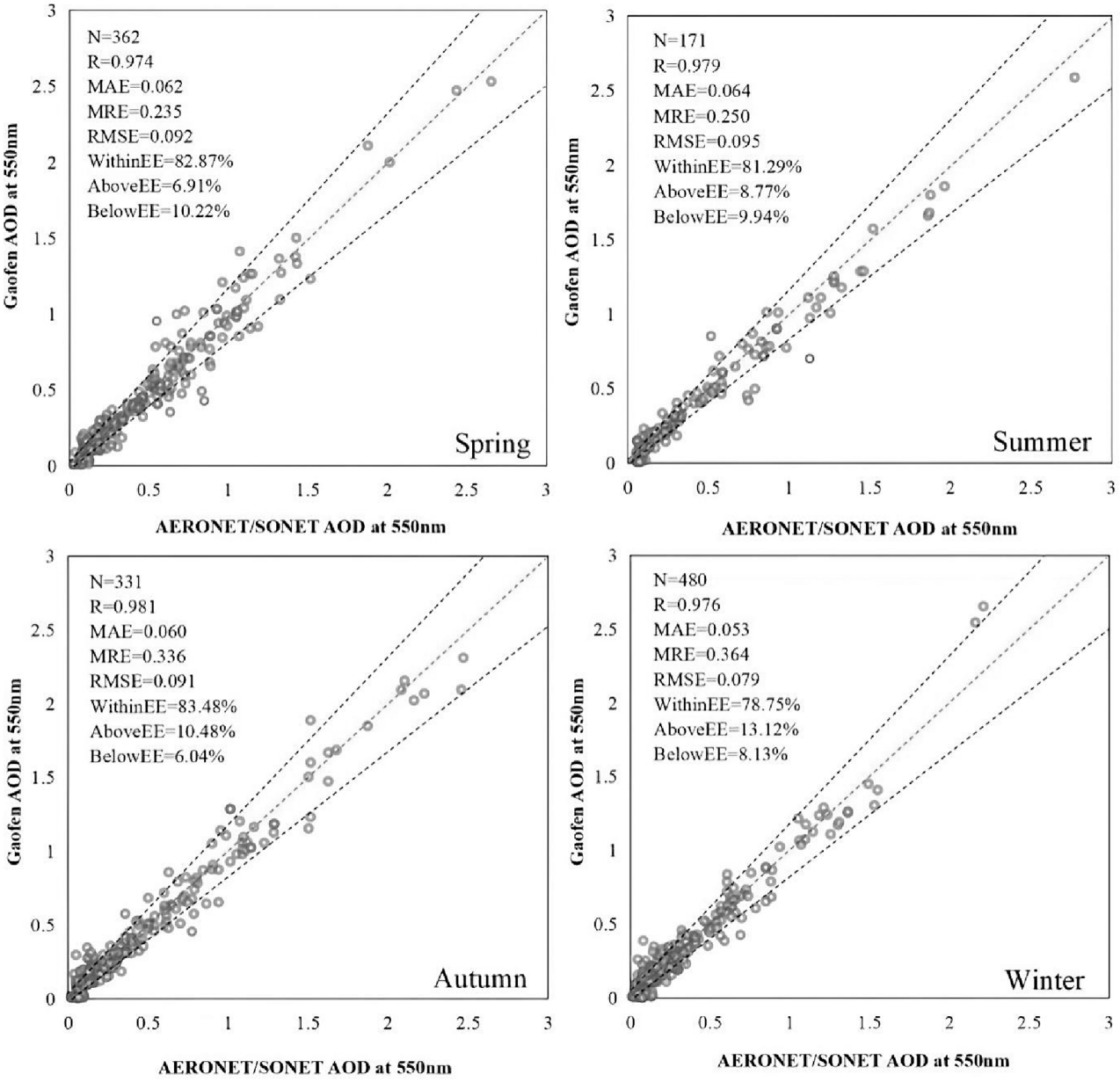

Fig. 8. Validation of the Gaofen WFV AOD retrievals against the AERONET/SONET AOD measurements over Beijing in different seasons from 2013 to 2020. Black dashed lines represent the EE envelope lines, and the red dashed lines are the 1:1 reference lines. (For interpretation of the references to color in this figure legend, the reader is referred to the web version of this article.)

retrieval scheme demonstrates the generally consistent performance between different satellites, which indicates the applicability of the synergistic observation algorithm for Gaofen-1 and Gaofen-6 in this study.

Fig. 6 depicts the performance of the WFV AOD retrieval algorithm across varying aerosol loading conditions. The overall results indicate that the retrieval algorithm performs well, where over 75 % of the AOD retrievals fall within the EE envelope under any aerosol loading conditions, with the mean AOD bias closing to zero. It is indicated that when the aerosol loadings are relatively small (AOD < 0.5), the retrieval uncertainties of WFV AOD remain at a low level, where the absolute values of AOD bias are generally less than 0.15 with MAE and RMSE less than 0.1, which are introduced by the slight errors in LSR estimations. The RRMSE value presents a significantly high value when the aerosol loadings are small (AOD < 0.2), however, the corresponding values of RMSE remain as low as that of other aerosol loadings, indicating the absolute uncertainties are still very low, although the relative uncertainty appears to be large. In addition, the AOD retrieval uncertainties exhibit a growing trend for the AOD bias, MAE, and RMSE, along with the increase of aerosol loading, which are probably caused by the errors from the monthly aerosol model assumption magnified with the aerosol loading increasing to a certain extent. And the AOD retrieval uncertainties for relatively larger aerosol loading conditions (AOD > 0.8) remain at a relatively low level, where the absolute values of the AOD bias are generally less than 0.3, with the MAE less than 0.15, the RMSE less than 0.2, the EE ratio reaching up to 87 %, which also suggest the reliability of large values in WFV AOD retrievals.

Fig. 7 depicts the performance of the WFV AOD retrieval algorithm for each year over the study period. The overall results demonstrate that the retrieval algorithm performs well, where over 75 % of the AOD retrievals fall within the EE envelope for each year, with the mean AOD bias closing to zero. And the values of evaluation metrics of RMSE and

MAE are both less than 0.1, indicating the small uncertainty of the retrieval algorithm throughout the study period. Moreover, the AOD retrieval uncertainties exhibit no obvious change with the time series, even subsequent to 2018 when the integration of Gaofen-6 observations into the synergistic observations, demonstrating the superiority of considering surface bidirectional reflectance effect and monthly aerosol modeling in the retrieval algorithm.

As illustrated in Fig. 8, the validation of WFV-derived AOD against AERONET/SONET AOD is further conducted in different seasons. Overall, the validation results show a good consistency between the WFV AOD retrievals and the AERONET/SONET AOD in all seasons, where the best correlation appears in autumn with the R over 0.98 and approximately 83 % matchups falling within the EE envelopes, followed by summer and spring. Although the validation results in winter obtain lower correlation coefficient and EE ratio compared to other seasons, which is probably attributed to the relatively sparse vegetation cover in winter slightly affecting the LSR estimation accuracy and subsequently impacting the AOD retrieval accuracy to a certain extent, yet over 78 % EE ratio and relatively low MAE, MRE and RMSE in winter also demonstrate the data accuracy reliability in scientific applications and analyses. Besides, fewer matchups (N) could be found in summer compared to the other three seasons, due to the relatively higher cloud coverage percentage reducing the available satellite aerosol observations in the summer of Beijing.

In summary, the validation results against AERONET and SONET AOD measurements demonstrate generally high accuracy metrics of WFV AOD retrievals in this study. The bias or errors in the WFV AOD retrievals may fluctuate under different land cover types, aerosol loading, and seasonal conditions. Still, these fluctuations are limited within a relatively small range, which suggests the errors from the SAS-MRPV LSR determination scheme and aerosol type assumption during the retrieval processes are relatively slight, further indicating the reliable and consistent performances of WFV AOD retrievals in this study.

4.2. Comparison of Gaofen WFV AOD with operational MODIS AOD products under different atmospheric pollution conditions

The WFV AOD retrievals with relatively high spatial resolution are supposed to possess huge potential and advantages in monitoring and analyzing air pollution within urban areas at a fine scale. As shown in Figs. 9-11, three typical cases under different air pollution extents, namely a clean day, a light polluted day, and a haze day, are selected as examples to illustrate the WFV AOD performances compared against the widely used MODIS operational AOD products with 10 km, 3 km, and 1 km spatial resolution, via DB, DT, and MAIAC aerosol retrieval algorithms, respectively.

As illustrated in Fig. 9, the case day on Oct. 17, 2018, is generally a clean day for Beijing, where the aerosol loadings at low levels appear in urban centers while the atmospheric pollution is mainly located in the Southern and Southeastern regions of Beijing. Both MODIS DB AOD (Fig. 9c) and DT AOD (Fig. 9d) data can capture this overall spatial distribution of aerosol loadings at a relatively large scale, however, they could hardly distinguish the finer spatial differences inside the urban centers due to their coarse spatial resolution. Besides, it could be found that part of the DB AOD retrievals is contaminated by the cloud which leads to the overestimation of DB AOD values spatially adjacent to the cloud, and there still exist data blanks in the DT AOD retrievals without cloud shielding to a certain extent, due to the limitation from DT algorithm over brighter land surface reflectance such as urban surfaces. As for the MAIAC AOD (Fig. 9e) with 1 km spatial resolution, it shows limited variations in AOD distribution and appears excessively smooth failing to capture spatial differences of aerosol loadings in this case. As

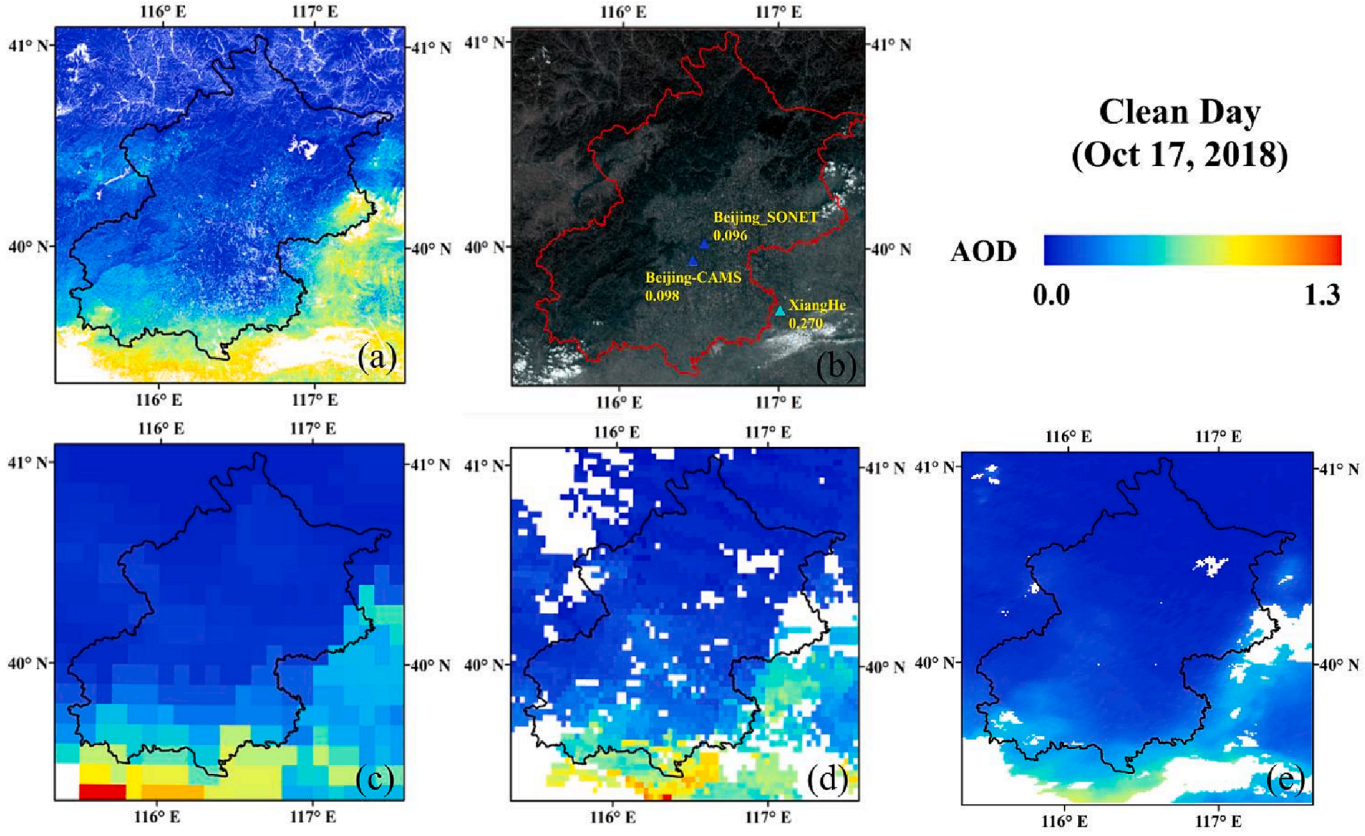

Fig. 9. Inter-comparison of (a) Gaofen WFV AOD (160 m) with MODIS (c) DB AOD (10 km), (d) DT AOD (3 km), (e) MAIAC AOD (1 km) at 550 nm on a clean day (Oct. 17, 2018), in conjunction with its corresponding MODIS-derived true-color image annotated with AERONET/SONET observation values (b). The color of triangle legends corresponds to the AOD value in color bar.

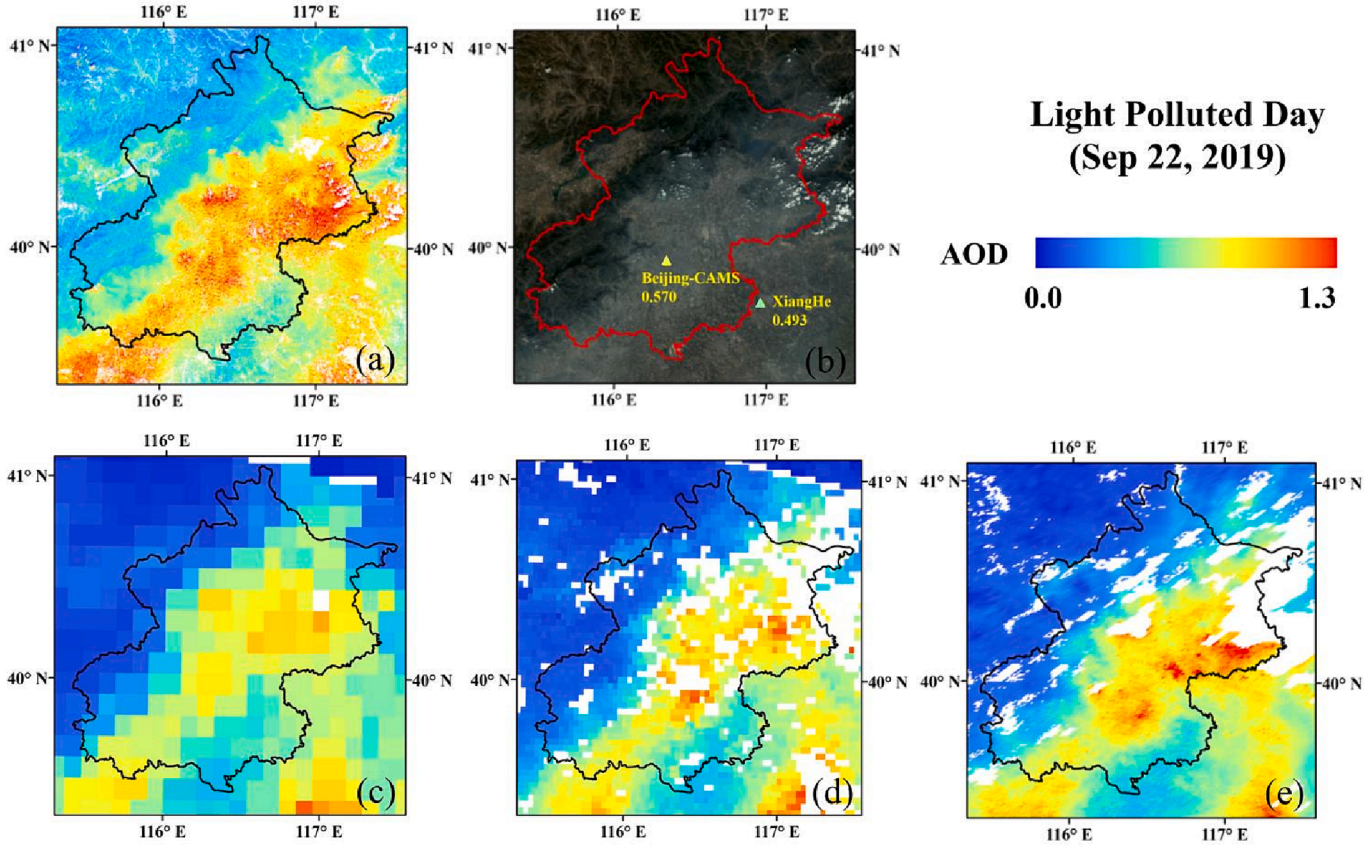

Fig. 10. Inter-comparison of (a) Gaofen WFV AOD (160 m) with MODIS (c) DB AOD (10 km), (d) DT AOD (3 km), (e) MAIAC AOD (1 km) at 550 nm on a light polluted day (Sep. 22, 2019), in conjunction with its corresponding MODIS-derived true-color image annotated with AERONET/SONET observation values(b). The color of triangle legends corresponds to the AOD value in color bar.

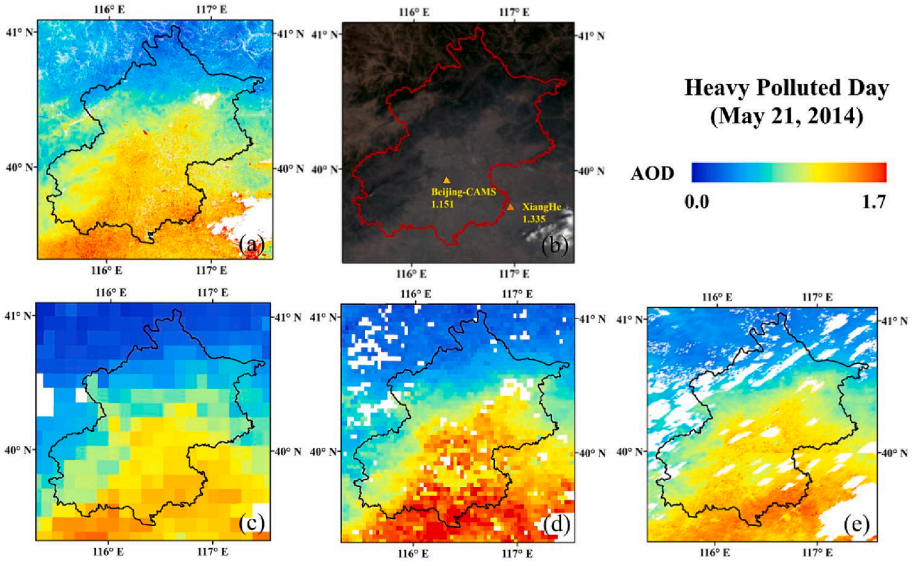

Fig. 11. Inter-comparison of (a) Gaofen WFV AOD (160 m) with MODIS (c) DB AOD (10 km), (d) DT AOD (3 km), (e) MAIAC AOD (1 km) at 550 nm on a haze day (May 21, 2014), in conjunction with its corresponding MODIS-derived true-color image annotated with AERONET/SONET observation values (b). The color of triangle legends corresponds to the AOD value in color bar.

contrast, the WFV AOD retrievals (Fig. 9a) in this case provide a finer description of aerosol spatial distribution with much more spatial details in the urban center, where the spatial differences of aerosol loadings within the central urban areas of Beijing can be observed that the AOD values from Inner Ring regions are generally lower than those from Outer Ring regions of Beijing, primarily caused by the varied densities of anthropogenic emissions. Moreover, the WFV AOD in this case illustrates its good performance in distinguishing the cloud pixels from aerosol pixels, and only a rather small proportion of data blanks appears in the WFV AOD data due to quality assurance during the retrieval

algorithm.

The Fig. 10 illustrates a light-polluted day on Sep. 22, 2019. Roughly speaking, the overall atmospheric pollution is located in the central urban areas and eastern regions of Beijing, which could be similarly depicted by both MODIS and WFV AOD data. Beyond the general illustration of aerosol spatial distribution, the MAIAC AOD (Fig. 10e) with 1 km spatial resolution possesses the capability to characterize the aerosol spatial distribution at a finer scale with more smooth variation details. And the WFV AOD (Fig. 10a) not only depicts the comprehensive spatial distribution of AOD but also provides the finest description of spatial characteristics of air pollution, which offers the possibility to assess the air pollution exposure and health risk at the community level (usually on the hundred-meter scale), benefit from its advantage in spatial resolution. Although it should be admitted that there exist few AOD abnormal values contaminated by sporadically shattered clouds in the WFV AOD retrievals, the percentage of data missing in the WFV AOD retrievals is obviously lower than in the MODIS DT and MAIAC AOD products.

As illustrated in Fig. 11, a haze case in Beijing is illustrated on May 21, 2014, when the whole urban area of Beijing suffered from severe atmospheric pollution. Both MODIS and WFV AOD datasets possess the ability to characterize the spatial distribution of extreme haze situations that the primary atmospheric pollution gathers in the North China Plain regions, and the pollution level is mitigated to some extent in Western and Northern regions blocked by mountains. Unlike MODIS DB and DT AOD products, the MODIS MAIAC AOD and WFV AOD data both characterize the aerosol spatial distribution with smooth variation attributable to higher spatial resolution. There are limited spatial variation details that can be observed from neither MODIS MAIAC 1 km AOD nor WFV 160 m AOD, since the atmospheric pollution tends to be more spatially uniform under severe haze conditions.

In summary, the inter-comparison between WFV-derived AOD against three operational MODIS AOD products demonstrates that the 160 m WFV AOD retrievals in this study not only obtain similar aerosol overall descriptions as MODIS AOD retrievals but also possess the capability to characterize the spatial distribution of atmospheric pollution at a finer scale with smoother variation under both clean and polluted conditions. Moreover, benefiting from its advantage in spatial resolution, the WFV AOD data could distinguish more delicate AOD spatial variation details, which offers the possibility to analyze the anthropogenic emissions or assess the air pollution exposure and health risks at a community level.

4.3. *Evaluation of potentials of the high spatial resolution WFV AOD in atmospheric pollution emission source tracking and analysis*

In addition to providing finer descriptions of aerosol spatial distribution, the 160 m WFV-derived AOD data retrieved in this study offers a possibility to identify and track the potential atmospheric pollution emission sources at a relatively small geographical scale. As illustrated in Fig. 12, the annually mean AOD in 2019, along with the single-day image on September 29, 2019, demonstrates that the annually mean AOD map provides a more comprehensive evaluation of the average annual emissions within specific emission areas, while the single-day map is effective in identifying atmospheric pollution emission sources that have significant emissions on that particular day. Furthermore, to demonstrate and evaluate the performances of tracking results, several typical polluted regions are selected and zoomed in upon, combined with corresponding Google Earth images provided as references. The selected polluted regions consist of the mining areas (region a in Fig. 12), the industrial factory (region b in Fig. 12), the residential and commercial hybrid areas (region c in Fig. 12), and the industrial parks (region d in Fig. 12). The results indicate that the industrial factory (Fig. 12 b2) and parks (Fig. 12 d2) possess a relatively higher pollution emission level compared to other regions, with the atmospheric pollution showing a diffusion pattern from emission center to the surrounding areas. Moreover, Fig. 12 a2 outlines a mining zone, where the pollution patterns demonstrate that there exist slightly higher AOD values in patches than the background AOD, which distinguishes the mining emissions areas from the vegetation fields. In addition to that, Fig. 12 c2 displays a residential and commercial areas, where it is found that the commercial areas possess relatively higher extents of pollution emissions than the residential areas.

Moreover, the potential atmospheric emission sources and corresponding emission levels derived from the WFV AOD map could be further verified by analyses incorporating the primary road network and the locations of key atmospheric pollution emission units, which serve as indicators of vehicle-generated and industrial atmospheric pollution, respectively. Collectively, it is indicated that the WFV-derived AOD map provides valuable insights into the identification of vehicle-related and industrial emission sources for better assessing their intra-city influences on atmospheric pollution. The geographic distribution of areas exhibiting higher AOD values closely aligns with regions characterized by elevated road network density. This correspondence suggests that AOD pollution resulting from transportation activities in Beijing is obvious. To be specific, the mining zone (Fig. 12 a2) stands out due to its relative

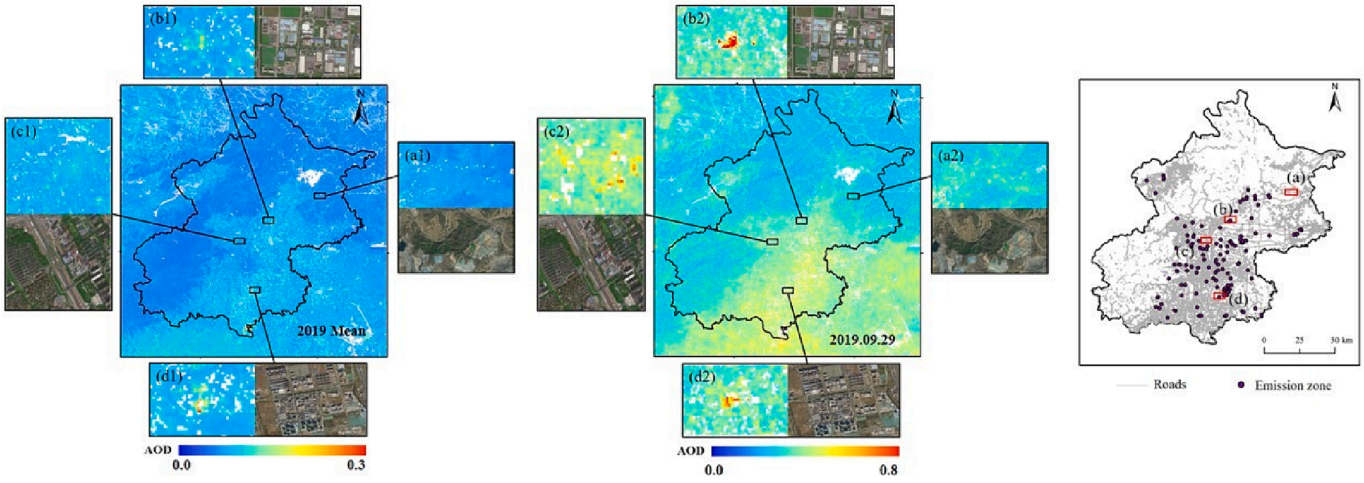

Fig. 12. Identification of the atmospheric pollution emission Sources via WFV AOD map in 2019 and on September 29, 2019. The subplots illustrate the detailed spatial distribution of AOD with their corresponding Google Earth images, including (a) Mining areas, (b) Industrial factories, (c) Residential and commercial hybrid areas, and (d) Industrial parks. Grey lines depict the spatial distribution of the primary road network, and purple dots illustrate the location of key atmospheric pollution emission units in Beijing. (For interpretation of the references to color in this figure legend, the reader is referred to the web version of this article.)

absence of proximate atmospheric emission sources and a sparsely interconnected road network. This distinction may be attributed to its suburban location, where the presence of both road networks and industrial emission units is limited. Consequently, the mining zone experiences less influence from these sources of pollution. Notably, this observation implies that the pollution in the vicinity of the mining site predominantly emanates from the substantial dust generated during the mining and ore processing activities, thus attributing the airborne pollution to the mining operations. In contrast, the other three regions located on impervious surfaces exhibit high road network density and proximity to significant emission sources. Regions b and d, in particular, are situated within emission units, with region c partially covered yet surrounded by numerous emission sources. Region c exhibits a dense road network, aligning with the observed distribution pattern of heightened AOD values compared to the background AOD within this area. However, the intensity of AOD pollution within the cores of regions b and d, which progressively diminishes towards their peripheries, provides further evidence of the spatial distribution characteristics of industrial-related atmospheric pollution. Additionally, region d features a denser road network compared to region b, resulting in a similar AOD pattern with localized increases in AOD values relative to the background AOD similar to region c. However, this phenomenon is absent in region b.

Thus, it is indicated that the WFV-derived AOD possesses the capability of accurately locating the atmospheric pollution emission sources and determining their emission levels at a fine scale, which could further support related research on community-level health risk assessments or urban climatology.

4.4. Error analysis and quality control in the SAS-MRPV scheme

In this study, the efficacy of the SAS-MRPV scheme in high-resolution land surface bidirectional reflectance description is evaluated using two metrics, namely the RMSE and the WoD, which are integrated into the operational product to measure and quantify the uncertainty associated with BRDF retrieval performance (Shuai et al., 2008). The RMSE measures the accuracy of the SAS-MRPV scheme, while the WoD serves as an indicative metric for the performance of kernel-driven linear models, particularly when confronted with limited and fluctuating angular samplings. The combined use of these two metrics during the SAS-MRPV scheme enables the quantification of LSR determination uncertainties.

Table 3 demonstrates the statistics metrics of RMSE and WoD in each seasonal LSR modeling for all the available pixels over natural and impervious land surfaces, respectively, where the mean RMSE and WoD indexes in the study areas range from 0.017 to 0.025 and 28.03 to 66.00, respectively. The RMSE and WoD of LSR modeling over impervious land surfaces are slightly higher than those over natural land surfaces, but the difference is not obvious, indicating that the developed SAS-MRPV scheme can achieve relatively stable performances under different land surface types including heterogeneous land surfaces with distinct anisotropy of bidirectional reflectance. Moreover, the RMSE and WoD indexes for LSR modeling in winter are not as good as those in the other three seasons, which could be probably caused by some areas being partly and occasionally covered by snow during the winter. This uncertain reflectance change from the land surfaces due to snow cover perturbations undoubtedly introduces uncertainties into the SAS-MRPV scheme, which yields relatively larger RMSE and WoD indexes observed during this period.

In this study, accordingly, the quality control for LSR modeling is conducted on each available land pixel through a combination of RMSE and WoD indexes. The SAS-MRPV scheme developed in this study employs the RMSE and WoD screening criteria to first determine the quality assurance (QA) for each effective LSR modeling pixel and then exclude pixels with margin QA flag, which aims to reduce uncertainty in the subsequent AOD retrieval processes. To be specific, pixels with RMSE values greater than 0.08 are initially excluded similar to prior studies (Hu et al., 1997; Lucht et al., 2000; Shuai et al., 2008), followed by consideration of the WoD values to screen the pixels with insufficient LSR modeling matchups. Moreover, seasonal upper thresholds for both RMSE and WoD indexes are determined at three times the standard deviation levels.

To evaluate the efficacy of quality control of the SAS-MRPV scheme on LSR modeling, Fig. 13 illustrates the performances of quality assurance screening by comparing land surface bidirectional reflectance results with all QA flags and with high QA flags. The left subplot in Fig. 13 shows the land surface bidirectional reflectance map over Beijing after quality control under a specific geometry situation on September 22, 2019. Three typical land surface types, which probably possess relatively large uncertainty during the LSR modeling, are selected, i.e., the mountain ridge lines (Fig. 13a), the Beijing Capital International Airport (Fig. 13b), and the water body/shore alternating surfaces (Fig. 13c). The mean RMSE and WoD of the mountain ridge line are 0.016 and 74.89, indicating a situation that the RMSE is small but the WoD is relatively too large, which may be due to the insufficient observation angle samples, as well as neglecting topographic effects similar with the RTLSR model (Hao et al., 2018; Hao et al., 2020a). The water body/shore alternating surfaces, which represent the areas that may alter to each other during different periods of abundance and depletion, demonstrate the mean RMSE and WoD are both relatively large, which is caused by dramatic surface bidirectional reflectance variations due to the change of land properties. Although the available WFV AOD retrieval pixels are restricted to cloud-free land surfaces that water body pixels have been screened out during the pixel selection process, it should be noted that the reflectivity of water body/shore alternating surfaces may not be uniformly described, making it difficult to identify accurately only depending on land cover datasets (Fig. 13 b2). In contrast, the quality control during the SAS-MRPV scheme can exclude these critical pixels and prevent them from retrieving aerosol information (Fig. 13 b3). The mean RMSE and WoD of the Beijing Capital International Airport reach 0.35 and 84.84, respectively, indicating the LSR modeling over strongly reflective land surfaces remains unreliable and needs to be screened to avoid error propagation in the subsequent AOD retrieval processes. Thus, it is indicated that the quality control procedure in the SAS-MRPV scheme is effective and necessary to guarantee the reliability and accuracy of land surface bidirectional reflectance estimation by identifying and excluding the land surface pixels unsuitable for LSR modeling,

Table 3
List of statistics metrics of RMSE and WoD in each season.

Land cover type	Season	RMSE				WoD			
		Min	Max	Mean	Std	Min	Max	Mean	Std
Natural Surface	Spring	0.005	0.080	0.020	0.004	5.393	79.985	46.950	10.729
	Summer	0.000	0.080	0.017	0.006	3.182	59.981	28.032	10.703
	Autumn	0.005	0.068	0.022	0.004	5.972	59.999	33.945	11.554
	Winter	0.007	0.056	0.024	0.004	4.712	99.999	57.161	13.188
Impervious Surface	Spring	0.008	0.076	0.025	0.003	9.127	79.999	58.996	7.349
	Summer	0.000	0.080	0.021	0.004	3.696	59.991	40.579	11.769
	Autumn	0.005	0.068	0.022	0.004	12.500	59.999	35.243	9.144
	Winter	0.007	0.056	0.024	0.004	10.112	99.999	65.333	10.851

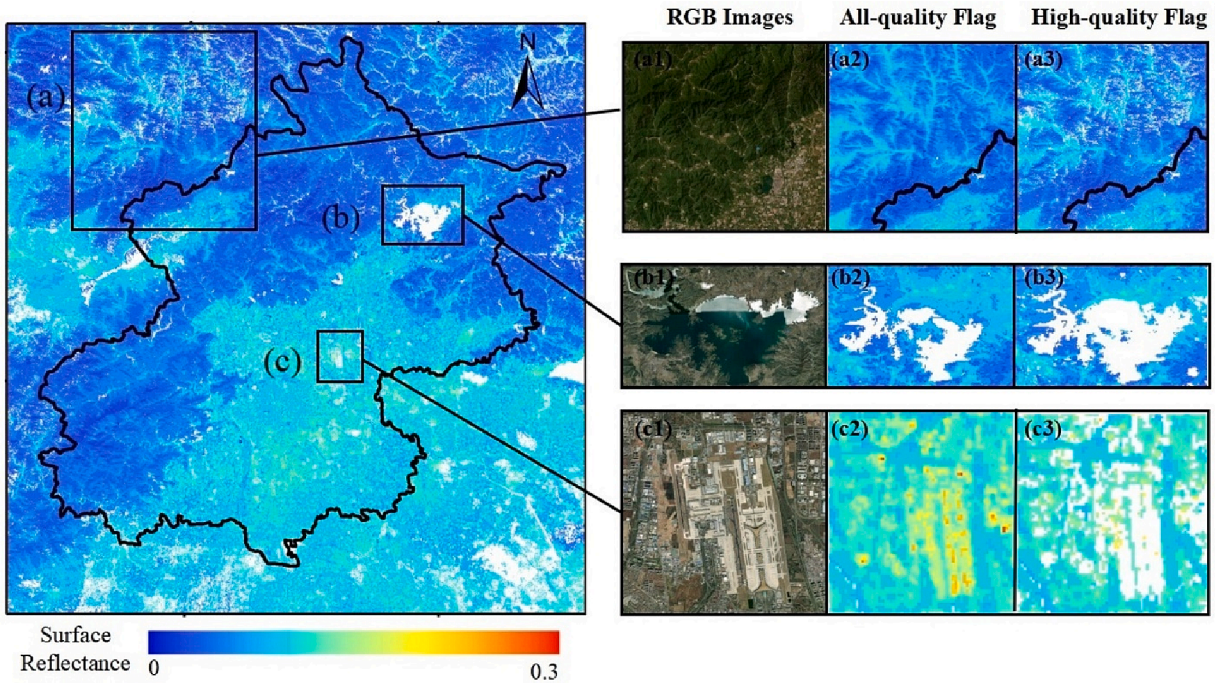

Fig. 13. The land surface bidirectional reflectance map over Beijing after quality assurance control using a combination of RMSE and WOD indexes under a specific geometry situation on September 22, 2019, combined with three detailed spatial distributions and corresponding Google Earth images, presenting three typical cases including (a) Mountain ridge line; (b) Water body/shore alternating surfaces; (c) Beijing Capital International Airport. The subplots (a1) – (c1) are the Google Earth Images used as location references. The subplots (a2) – (c2) are the land surface bidirectional reflectance before quality control with both high and margin quality assurances. The subplots (a3) – (c3) are the land surface bidirectional reflectance after quality control with only high-quality assurance.

which mitigates the uncertainty and yield better accuracy in the final WFV AOD products.

5. Conclusion

In order to yield a daily AOD dataset over urban areas with 160 m spatial resolution, this study develops a comprehensive AOD retrieval framework starting from DN values for WFV sensors based on synergistic observations from Gaofen-1 and Gaofen-6. This retrieval framework firstly includes a series of preprocessing algorithms, such as cloud/cloud-shadow mask, snow/ice surface screening, precise geometric correction, cross-radiation calibration, pixel integration, etc., to ensure the reliability of pixels used in the subsequent LSR determination and AOD retrieval procedures. Moreover, to address the crucial challenge that the high spatial resolution and complex urban landscape both contribute a dramatic variation of land surface bidirectional reflectance, a novel SAS-MRPV scheme is proposed to characterize and model the LSR over urban areas, combined with the corresponding quality control via two evaluation metrics, namely RMSE and WoD. The SAS-MRPV LSR scheme is implemented by achieving global optimization for the semi-empirical MRPV BRDF model by using simulated annealing iteration, which is initialized by the MODIS BRDF parameters as a priori knowledge to obviously improve the convergence efficiency and fitting accuracy. And the AOD retrieval is accordingly conducted by utilizing optimal interpolation on the constructed LUT based on particular monthly aerosol models. The validation results demonstrate that the Gaofen WFV AOD retrievals possess consistent performances with ground-based AERONET/SONET AOD measurements, where the correlation coefficient attains an impressive 0.97, and the EE ratio approaches over 80 %. The bias fluctuations in the WFV AOD retrievals are found to be limited within a relatively small range under different land cover types, aerosol loading, and seasonal conditions, which suggests the constrained errors in the SAS-MRPV LSR determination scheme and aerosol type assumption during the retrieval processes, further indicating the reliable and consistent performances of WFV AOD retrievals. Moreover, the validation results of Gaofen WFV AOD retrievals, with LSR estimated based on the SAS-MRPV scheme, the MODIS BRDF Products, and the MRT method, demonstrate better accuracy and completeness of AOD retrievals through LSR estimated based on the SAS-MPRV scheme over both natural and impervious land surfaces, indicating the stability and reliability of proposed SAS-MRPV LSR determination scheme in WFV AOD retrieval. Furthermore, the error analyses and quality control results demonstrate that the SAS-MRPV scheme is effective and necessary to guarantee the reliability and accuracy of land surface bidirectional reflectance estimation by identifying and excluding the land surface pixels unsuitable for LSR modeling, which mitigates the uncertainty and yield better accuracy in the final WFV AOD products. Furthermore, the inter-comparison between WFV-derived AOD against the operational MODIS DB (10 km), DT (3 km), and MAIAC (1 km) AOD products demonstrates that the 160 m WFV AOD retrievals in this study not only obtain similar aerosol overall descriptions as MODIS AOD retrievals, but also possess the capability to characterize the spatial distribution of atmospheric pollution at a finer scale with smoother variation under both clean and polluted conditions. Benefiting from its advantage in spatial resolution, it is illustrated that the WFV-derived AOD possesses the capability of accurately locating the atmospheric pollution emission sources and determining their emission levels at a fine scale, which could provide fundamental data support to related research on community-level health risk assessments or urban climatology.

As a first attempt to simultaneously achieve high spatial resolution and ideal temporal resolution in satellite-derived aerosol observations, we select Beijing as a representative megacity to obtain a daily 160 m AOD dataset over Beijing based on Gaofen-1/6 synergistic observations, where over 250 days of valid AOD maps with less than 80 % cloud obscuration could be yielded in one year as shown in Supplementary Materials Figure S2. With outstanding accuracy and reliable performance, the developed comprehensive high-resolution AOD retrieval

framework exhibits substantial potential for operational AOD retrieval of Gaofen WFV satellite measurements. Considering huge amount data capacity and the time-consuming algorithm processing procedures for Gaofen-1/6, we will gradually yield and release the 160 m AOD products for other cities worldwide, combined with corresponding validations for data accuracy and reliability, to further demonstrate the generalization of the developed aerosol retrieval algorithm. To guarantee the daily revisiting observation period even if some cities are in low latitudes, we plan to expand the high-resolution AOD retrieval algorithm to other satellite sensors like Landsat-7/8 and Sentinel-2, which possess similar spectral bands as Gaofen-series, to construct a high spatial resolution aerosol monitoring network, for supporting further studies related to air pollution emission management and health risk assessment at extra-fine spatial scale over urban areas. Admittedly, several issues worthy further consideration should be mentioned. First, a more accurate aerosol model determination scheme could be adopted to further decrease the uncertainty in AOD retrieval, considering the complexity and variability of aerosol components. Moreover, the uncertainty in AOD retrieval includes uncertainty arising from the calculation for Rayleigh scattering and absorption of ozone, water vapor and nitrogen oxide (Zhang et al., 2013). The ozone and water vapor have been customized in 6SV LUT for AOD retrieval in this study. For future studies, the possible improvement for WFV AOD retrieval algorithm can be achieved by using a more accurate characterization of nitrogen oxide to decrease the uncertainties introduced by determined atmospheric model assumption (Drosoglou et al., 2023), particularly in some regions periodically suffering from NO_2 pollution such as China. Furthermore, considering that the 470 nm wavelength becomes sensitive to aerosol height with increasing AOD (Li et al., 2020), a more accurate vertical distribution of aerosol profile could be introduced into the atmospheric radiative model in future work to further reduce the uncertainty in AOD retrieval.

CRediT authorship contribution statement

Jiadan Dong: Conceptualization, Methodology, Validation, Visualization, Writing – original draft, Writing – review & editing. **Tianhao Zhang:** Conceptualization, Methodology, Supervision, Validation, Writing – original draft, Writing – review & editing. **Lunche Wang:** Conceptualization, Methodology, Writing – review & editing. **Zhengqiang Li:** Methodology, Writing – review & editing. **Man Sing Wong:** Conceptualization, Methodology, Writing – review & editing. **Muhammad Bilal:** Conceptualization, Methodology, Writing – review & editing. **Zhongmin Zhu:** Conceptualization, Methodology, Supervision, Writing – review & editing. **Feiyue Mao:** Validation, Writing – review & editing. **Xinghui Xia:** Conceptualization, Methodology, Writing – review & editing. **Ge Han:** Validation, Writing – review & editing. **Qiangqiang Xu:** Validation, Writing – review & editing. **Yu Gu:** Writing – review & editing, Validation. **Yun Lin:** Writing – review & editing, Validation. **Bin Zhao:** Writing – review & editing, Validation. **Zhiwei Li:** Methodology, Writing – review & editing. **Kai Xu:** Methodology, Writing – review & editing. **Xiaoling Chen:** Supervision, Validation, Writing – review & editing. **Wei Gong:** Supervision, Validation, Writing – review & editing.

Declaration of competing interest

The authors declare that they have no known competing financial interests or personal relationships that could have appeared to influence the work reported in this paper.

Acknowledgment

This work was financially supported by the National Natural Science Foundation of China (No. 42071353), and the China Postdoctoral Science Foundation (No. 2020M682486). The authors would like to express their gratitude to the China Centre for Resources Satellite Data and Application for providing the Gaofen-1/6 WFV Level 1 data, the NASA for providing several Terra/Aqua MODIS products, the NASA/USGS Landsat Science Team for providing Landsat-8 OLI data, the ECMWF for providing the meteorological reanalysis datasets, and the Principle Investigators for establishing and maintaining the AERONET network.

Appendix A. Supplementary data

Supplementary data to this article can be found online at https://doi.org/10.1016/j.isprsjprs.2024.04.020.

References

Anderson, T.L., Charlson, R.J., Bellouin, N., Boucher, O., Chin, M., Christopher, S.A., Haywood, J., Kaufman, Y.J., Kinne, S., Ogren, J.A., Remer, L.A., Takemura, T., Tanre, D., Torres, O., Trepte, C.R., Wielicki, B.A., Winker, D.M., Yu, H.B., 2005. An "A-Train" strategy for quantifying direct climate forcing by anthropogenic aerosols. Bull. Am. Meteorol. Soc. 86, 1795–1809.

Armston, J.D., Scarth, P.F., Phinn, S.R., Danaher, T.J., 2007. Analysis of multi-date MISR measurements for forest and woodland communities, Queensland, Australia. Remote Sens. Environ. 107, 287–298.

Bendixen, M., Jorgensen, O.D., Kronborg, C., Andersen, C., Licht, P.B., 2016. Postoperative pain and quality of life after lobectomy via video-assisted thoracoscopic surgery or anterolateral thoracotomy for early stage lung cancer: a randomised controlled trial. Lancet Oncol. 17, 836–844.

Bilal, M., Nazeer, M., Nichol, J., Qiu, Z.F., Wang, L.C., Bleiweiss, M.P., Shen, X.J., Campbell, J.R., Lolli, S., 2019. Evaluation of Terra-MODIS C6 and C6.1 Aerosol Products against Beijing, XiangHe, and Xinglong AERONET Sites in China during 2004–2014. Remote Sens. (Basel) 11.

Bilal, M., Nichol, J.E., 2015. Evaluation of MODIS aerosol retrieval algorithms over the Beijing-Tianjin-Hebei region during low to very high pollution events. J. Geophys. Res.-Atmos. 120, 7941–7957.

Bilal, M., Nichol, J.E., Bleiweiss, M.P., Dubois, D., 2013. A Simplified high resolution MODIS Aerosol Retrieval Algorithm (SARA) for use over mixed surfaces. Remote Sens. Environ. 136, 135–145.

Bilal, M., Nichol, J.E., Chan, P.W., 2014. Validation and accuracy assessment of a Simplified Aerosol Retrieval Algorithm (SARA) over Beijing under low and high aerosol loadings and dust storms. Remote Sens. Environ. 153, 50–60.

Bilal, M., Nichol, J.E., Wang, L., 2017. New customized methods for improvement of the MODIS C6 Dark Target and Deep Blue merged aerosol product. Remote Sens. Environ. 197, 115–124.

Bilal, M., Qiu, Z.F., Nichol, J.E., Mhawish, A., Ali, M.A., Khedher, K.M., de Leeuw, G., Yu, W., Tiwari, P., Nazeer, M., Bleiweiss, M.P., 2022. Uncertainty in Aqua-MODIS Aerosol Retrieval Algorithms During COVID-19 Lockdown. IEEE Geosci. Remote Sens. Lett. 19.

Boiyo, R., Kumar, K.R., Zhao, T.L., 2018. Spatial variations and trends in AOD climatology over East Africa during 2002–2016: a comparative study using three satellite data sets. Int. J. Climatol. 38, E1221–E1240.

Boys, B.L., Martin, R.V., van Donkelaar, A., MacDonell, R.J., Hsu, N.C., Cooper, M.J., Yantosca, R.M., Lu, Z., Streets, D.G., Zhang, Q., Wang, S.W., 2014. Fifteen-Year Global Time Series of Satellite-Derived Fine Particulate Matter. Environ. Sci. Tech. 48, 11109–11118.

Cai, S., Ren, Q.Q., Zeng, Y.A., Wang, L.G., Zhang, Y.Z., Liu, B., Li, J.G., 2021. Toxicity assessment of the utilization of AOD slag as a mineral fertilizer for pakchoi (Brassica chinensis L.) planting. J. Clean. Prod. 328.

Carabali, G., Estevez, H.R., Valdes-Barron, M., Bonifaz-Alfonzo, R., Riveros-Rosas, D., Velasco-Herrera, V.M., Vazquez-Galvez, F.A., 2017. Aerosol climatology climatology over the Mexico City basin: Characterization of optical properties. Atmos. Res. 194, 190–201.

Cheng, T., Gu, X., Xie, D., Li, Z., Yu, T., Chen, H., 2012. Aerosol optical depth and fine-mode fraction retrieval over East Asia using multi-angular total and polarized remote sensing. Atmos. Meas. Tech. 5, 501–516.

Dong, J., Cai, X., Tian, L., Chen, F., Xu, Q., Li, T., Chen, X., 2023a. Satellite-based estimates of daily NO2 exposure in urban agglomerations of China and application to spatio-temporal characteristics of hotspots. Atmos. Environ. 293.

Dong, J.D., Chen, Y.P., Chen, X.L., Xu, Q.Q., 2023b. Radiometric Cross-Calibration of Wide-Field-of-View Cameras Based on Gaofen-1/6 Satellite Synergistic Observations Using Landsat-8 Operational Land Imager Images: A Solution for Off-Nadir Wide-Field-of-View Associated Problems. Remote Sens. (Basel) 15.

Dong, Z.P., Liu, Y.X., Xu, W.X., Feng, Y.K., Chen, Y.L., Tang, Q.H., 2021. A cloud detection method for GaoFen-6 wide field of view imagery based on the spectrum and variance of superpixels. Int. J. Remote Sens. 42, 6315–6332.

Drosoglou, T., Raptis, I.P., Valeri, M., Casadio, S., Barnaba, F., Herreras-Giralda, M., Lopatin, A., Dubovik, O., Brizzi, G., Niro, F., Campanelli, M., Kazadzis, S., 2023. Evaluating the effects of columnar NO₂ on the accuracy of aerosoloptical properties retrievals. Atmos. Meas. Tech. 16, 2989–3014.

Du, X.P., Guo, H.D., Fan, X.T., Zhu, J.J., Yan, Z.Z., Zhan, Q., 2016. Vertical accuracy assessment of freely available digital elevation models over low-lying coastal plains. Int. J. Digital Earth 9, 252–271.

Eck, T.F., Holben, B.N., Giles, D.M., Slutsker, I., Sinyuk, A., Schafer, J.S., Smirnov, A., Sorokin, M., Reid, J.S., Sayer, A.M., Hsu, N.C., Shi, Y.R., Levy, R.C., Lyapustin, A., Rahman, M.A., Liew, S.C., Cortijo, S.S., Li, T., Kalbermatter, D., Keong, K.L.,

Yuggotomo, M.E., Aditya, F., Mohamad, M., Mahmud, M., Chong, T.K., Lim, H.S., Choon, Y.E., Deranadyan, G., Kusumaningtyas, S.D.A., Aldrian, E., 2019. AERONET Remotely Sensed Measurements and Retrievals of Biomass Burning Aerosol Optical Properties During the 2015 Indonesian Burning Season. J. Geophys. Res.-Atmos. 124, 4722–4740.

El-Metwally, M., Alfaro, S.C., Wahab, M.M.A., Favez, O., Mohamed, Z., Chatenet, B., 2011. Aerosol properties and associated radiative effects over Cairo (Egypt). Atmos. Res. 99, 263–276.

Engelsen, O., Pinty, B., Verstraete, M.M., & Martonchik, J.V. (1998). Parametric surface bidirectional reflectance factor models for atmospheric radiative transfer modeling. In, *1998 International Geoscience and Remote Sensing Symposium (IGARSS 98) on Sensing and Managing the Environment* (pp. 713-715). Seattle, Wa.

Engelsen, O., Pinty, B., Verstraete, M.M., Martonchik, J.V., 1997. Design and evaluation of parametric bidirectional reflectance factor models. In: *7th International Symposium on Physical Measurements and Signatures in Remote Sensing, Courchevel, France*, pp. 219–225.

Fan, R.A., Ma, Y.Y., Jin, S.K., Gong, W., Liu, B.M., Wang, W.Y., Li, H., Zhang, Y.Q., 2023. Validation, analysis, and comparison of MISR V23 aerosol optical depth products with MODIS and AERONET observations. Sci. Total Environ. 856.

Feng, L., Li, J., Gong, W.S., Zhao, X., Chen, X.L., Pang, X.P., 2016. Radiometric cross-calibration of Gaofen-1 WFV cameras using Landsat-8 OLI images: A solution for large view angle associated problems. Remote Sens. Environ. 174, 56–68.

Feng, S.S., Lin, Y., Hong, W., Han, B., Wang, Y.P., Yang, Y.H., Shen, W.J., Teng, F., IEEE, 2019. DEM extraction using C-band circular SAR data. In: IEEE International Geoscience and Remote Sensing Symposium (IGARSS), Yokohama, Japan, pp. 552–555.

Ge, B.Y., Li, Z.Q., Liu, L., Yang, L.K., Chen, X.F., Hou, W.Z., Zhang, Y., Li, D.H., Li, L., Qie, L.L., 2019. A Dark Target Method for Himawari-8/AHI Aerosol Retrieval: Application and Validation. IEEE Trans. Geosci. Remote Sens. 57, 381–394.

Gillingham, S.S., Flood, N., Gill, T.K., Mitchell, R.M., 2012. Limitations of the dense dark vegetation method for aerosol retrieval under Australian conditions. Remote Sensing Letters 3, 67–76.

Gong, P., Li, X.C., Zhang, W., 2019. 40-Year (1978–2017) human settlement changes in China reflected by impervious surfaces from satellite remote sensing. Science Bulletin 64, 756–763.

Gui, K., Che, H.Z., Wang, Y.Q., Xia, X.A., Holben, B.N., Goloub, P., Cuevas-Agullo, E., Yao, W.R., Zheng, Y., Zhao, H.J., Li, L., Zhang, X.Y., 2021. A global-scale analysis of the MISR Level-3 aerosol optical depth (AOD) product: Comparison with multi-platform AOD data sources. Atmospheric. Pollut. Res. 12.

Guo, J.P., Niu, T., Wang, F., Deng, M.J., Wang, Y.Q., 2013. Integration of multi-source measurements to monitor sand-dust storms over North China: A case study. Acta. Meteor. Sin. 27, 566–576.

Hao, Y., Hao, X.Y., Li, Y.W., Zhang, Y.R., Wu, H.T., 2020b. How does air quality affect the willingness of graduate students to stay? Evidence from Beijing city, China. J. Clean. Prod. 259.

Hao, D.L., Wen, J.G., Xiao, Q., Wu, S.B., Lin, X.W., You, D.Q., Tang, Y., 2018. Modeling Anisotropic Reflectance Over Composite Sloping Terrain. IEEE Trans. Geosci. Remote Sens. 56, 3903–3923.

Hao, D.L., Wen, J.G., Xiao, Q., You, D.Q., Tang, Y., 2020a. An Improved Topography-Coupled Kernel-Driven Model for Land Surface Anisotropic Reflectance. IEEE Trans. Geosci. Remote Sens. 58, 2833–2847.

He, T., Liang, S.L., Wang, D.D., Cao, Y.F., Gao, F., Yu, Y.Y., Feng, M., 2018. Evaluating land surface albedo estimation from Landsat MSS, TM, ETM plus, and OLI data based on the unified direct estimation approach. Remote Sens. Environ. 204, 181–196.

Hersbach, H., Bell, B., Berrisford, P., Hirahara, S., Horanyi, A., Munoz-Sabater, J., Nicolas, J., Peubey, C., Radu, R., Schepers, D., Simmons, A., Soci, C., Abdalla, S., Abellan, X., Balsamo, G., Bechtold, P., Biavati, G., Bidlot, J., Bonavita, M., De Chiara, G., Dahlgren, P., Dee, D., Diamantakis, M., Dragani, R., Flemming, J., Forbes, R., Fuentes, M., Geer, A., Haimberger, L., Healy, S., Hogan, R.J., Holm, E., Janiskova, M., Keeley, S., Laloyaux, P., Lopez, P., Lupu, C., Radnoti, G., de Rosnay, P., Rozum, I., Vamborg, F., Villaume, S., Thepaut, J.N., 2020. The ERA5 global reanalysis. Q. J. R. Meteorolog. Soc. 146, 1999–2049.

Holben, B.N., Eck, T.F., Slutsker, I., Tanre, D., Buis, J.P., Setzer, A., Vermote, E., Reagan, J.A., Kaufman, Y.J., Nakajima, T., Lavenu, F., Jankowiak, I., Smirnov, A., 1998. AERONET - A federated instrument network and data archive for aerosol characterization. Remote Sens. Environ. 66, 1–16.

Holben, B., Vermote, E., Kaufman, Y.J., Tanre, D., Kalb, V., 1992. Aerosol retrieval over land from AVHRR Data - Application for atmospheric correctioN. IEEE Trans. Geosci. Remote Sens. 30, 212–222.

Hsu, N.C., Gautam, R., Sayer, A.M., Bettenhausen, C., Li, C., Jeong, M.J., Tsay, S.C., Holben, B.N., 2012. Global and regional trends of aerosol optical depth over land and ocean using SeaWiFS measurements from 1997 to 2010. Atmos. Chem. Phys. 12, 8037–8053.

Hsu, N.C., Lee, J., Sayer, A.M., Kim, W., Bettenhausen, C., Tsay, S.C., 2019. VIIRS Deep Blue Aerosol Products Over Land: Extending the EOS Long-Term Aerosol Data Records. J. Geophys. Res.-Atmos. 124, 4026–4053.

Hu, B.X., Lucht, W., Li, X.W., Strahler, A.H., 1997. Validation of kernel-drives semiempirical models for the surface bidirectional reflectance distribution function of land surfaces. Remote Sens. Environ. 62, 201–214.

Hu, R.L., Xu, Q.C., Wang, S.X., Hua, Y., Bhattarai, N., Jiang, J.K., Song, Y., Daellenbach, K.R., Qi, L., Prevot, A.S.H., Hao, J.M., 2020. Chemical characteristics and sources of water-soluble organic aerosol in southwest suburb of Beijing. J. Environ. Sci. 95, 99–110.

Jiang, X.X., Xue, Y., Jin, C.L., Bai, R., Sun, Y.X., & Wu, S.H. (2022). A Simple Band Ratio Library (BRL) Algorithm for Retrieval of Hourly Aerosol Optical Depth Using FY-4A AGRI Geostationary Satellite Data. *Remote Sensing, 14*.

Jiao, Z.T., Hill, M.J., Schaaf, C.B., Zhang, H., Wang, Z.S., Li, X.W., 2014. An Anisotropic Flat Index (AFX) to derive BRDF archetypes from MODIS. Remote Sens. Environ. 141, 168–187.

Jin, Z.Y., Xia, S., Cao, H.H., Geng, X.H., Cheng, Z.M., Sun, H.B., Jia, M.L., Liu, Q.Y., Sun, J., 2022. Evaluation and Optimization of Sustainable Development Level of Construction Industrialization: Case Beijing-Tianjin-Hebei Region. Sustainability 14.

Kaufman, Y.J., Tanre, D., Boucher, O., 2002. A satellite view of aerosols in the climate system. Nature 419, 215–223.

Kim, D., Kim, J., Jeong, J., Choi, M., 2019. Estimation of health benefits from air quality improvement using the MODIS AOD dataset in Seoul, Korea. Environ. Res. 173, 452–461.

Kinne, S., O'Donnel, D., Stier, P., Kloster, S., Zhang, K., Schmidt, H., Rast, S., Giorgetta, M., Eck, T.F., Stevens, B., 2013. MAC-v1: A new global aerosol climatology for climate studies. J. Adv. Model. Earth Syst. 5, 704–740.

Kumar, M., Parmar, K.S., Kumar, D.B., Mhawish, A., Broday, D.M., Mall, R.K., Banerjee, T., 2018. Long-term aerosol climatology over Indo-Gangetic Plain: Trend, prediction and potential source fields. Atmos. Environ. 180, 37–50.

Lautenschlager, F., Becker, M., Kobs, K., Steininger, M., Davidson, P., Krause, A., Hotho, A., 2020. OpenLUR: Off-the-shelf air pollution modeling with open features and machine learning. Atmos. Environ. 233.

Lee, J., Koo, J.H., Kim, S.M., Lee, T., Lee, Y.G., 2021. Comparison of Aerosol Properties in the Korean Peninsula Between AERONET Version 2 and 3 Data Set. Asia-Pac. J. Atmos. Sci. 57, 629–643.

Lelieveld, J., Beirle, S., Hormann, C., Stenchikov, G., Wagner, T., 2015. Abrupt recent trend changes in atmospheric nitrogen dioxide over the Middle East. *Science*. Advances 1.

Levy, R.C., Remer, L.A., Kleidman, R.G., Mattoo, S., Ichoku, C., Kahn, R., Eck, T.F., 2010. Global evaluation of the Collection 5 MODIS dark-target aerosol products over land. Atmos. Chem. Phys. 10, 10399–10420.

Levy, R.C., Mattoo, S., Munchak, L.A., Remer, L.A., Sayer, A.M., Patadia, F., Hsu, N.C., 2013. The Collection 6 MODIS aerosol products over land and ocean. Atmos. Meas. Tech. 6, 2989–3034.

Levy, R.C., Munchak, L.A., Mattoo, S., Patadia, F., Remer, L.A., Holz, R.E., 2015. Towards a long-term global aerosol optical depth record: applying a consistent aerosol retrieval algorithm to MODIS and VIIRS-observed reflectance. Atmos. Meas. Tech. 8, 4083–4110.

Li, C., Li, J., Dubovik, O., Zeng, Z.C., Yung, Y.L., 2020. Impact of Aerosol Vertical Distribution on Aerosol Optical Depth Retrieval from Passive Satellite Sensors. Remote Sens. (Basel) 12.

Li, J.Y., Schroder, S.E., Mottola, S., Nathues, A., Castillo-Rogez, J.C., Schorghofer, N., Williams, D.A., Ciamiello, M., Longobardo, A., Raymond, C.A., Russell, C.T., 2019. Spectrophotometric-modeling and mapping of Ceres. Icarus 322, 144–167.

Li, Z., Shen, H., Li, H., Xia, G., Gamba, P., Zhang, L., 2017. Multi-feature combined cloud and cloud shadow detection in GaoFen-1 wide field of view imagery. Remote Sens. Environ. 191, 342–358.

Li, Y.J., Xue, Y., He, X.W., Guang, J., 2012. High-resolution aerosol remote sensing retrieval over urban areas by synergetic use of HJ-1 CCD and MODIS data. Atmos. Environ. 46, 173–180.

Lin, H., Li, S.W., Xing, J., Yang, J., Wang, Q.X., Dong, L.C., Zeng, X.Y., 2021. Fusing Retrievals of High Resolution Aerosol Optical Depth from Landsat-8 and Sentinel-2 Observations over Urban Areas. Remote Sens. (Basel) 13.

Lin, X.W., Wu, S.B., Chen, B., Lin, Z.Y., Yan, Z.B., Chen, X.Z., Yin, G.F., You, D.Q., Wen, J. G., Liu, Q., Xiao, Q., Liu, Q.H., Lafortezza, R., 2022. Estimating 10-m land surface albedo from Sentinel-2 satellite observations using a direct estimation approach with Google Earth Engine. ISPRS J. Photogramm. Remote Sens. 194, 1–20.

Liu, J.J., Huang, J.P., Chen, B., Zhou, T., Yan, H.R., Jin, H.C., Huang, Z.W., Zhang, B.D., 2015. Comparisons of PBL heights derived from CALIPSO and ECMWF reanalysis data over China. J. Quant. Spectrosc. Radiat. Transf. 153, 102–112.

Liu, L.Y., Liu, X.J., Wang, Z.H., Zhang, B., 2016. Measurement and Analysis of Bidirectional SIF Emissions in Wheat Canopies. IEEE Trans. Geosci. Remote Sens. 54, 2640–2651.

Lucht, W., Lewis, P., 2000. Theoretical noise sensitivity of BRDF and albedo retrieval from the EOS-MODIS and MISR sensors with respect to angular sampling. Int. J. Remote Sens. 21, 81–98.

Lucht, W., Schaaf, C.B., Strahler, A.H., 2000. An algorithm for the retrieval of albedo from space using semiempirical BRDF models. IEEE Trans. Geosci. Remote Sens. 38, 977–998.

Lyapustin, A., Martonchik, J., Wang, Y.J., Laszlo, I., Korkin, S., 2011. Multiangle implementation of atmospheric correction (MAIAC): 1. Radiative transfer basis and look-up tables. J. Geophys. Res.-Atmos. 116.

Lyapustin, A., Wang, Y.J., Korkin, S., Huang, D., 2018. MODIS Collection 6 MAIAC algorithm. Atmos. Meas. Tech. 11, 5741–5765.

Ma, Y., Li, Z.Q., Li, Z.Z., Xie, Y.S., Fu, Q.Y., Li, D.H., Zhang, Y., Xu, H., Li, K.T., 2016. Validation of MODIS Aerosol Optical Depth Retrieval over Mountains in Central China Based on a Sun-Sky Radiometer Site of SONET. Remote Sens. (Basel) 8.

Mafarja, M.M., Mirjalili, S., 2017. Hybrid Whale Optimization Algorithm with simulated annealing for feature selection. Neurocomputing 260, 302–312.

Meng, K., Xu, X.D., Xu, X.B., Wang, H.L., Liu, X.H., Jiao, Y.Y., 2019. The Causes of "Vulnerable Regions" to Air Pollution in Winter in the Beijing-Tianjin-Hebei Region: A Topographic-Meteorological Impact Model Based on Adaptive Emission Constraint Technique. Atmos. 10.

Mou, H.W., Li, H., Zhou, Y.G., Dong, R.J., 2021. Response of Different Band Combinations in Gaofen-6 WFV for Estimating of Regional Maize Straw Resources Based on Random Forest Classification. Sustainability 13.

Nguyen, H.M., Wooster, M.J., 2020. Advances in the estimation of high Spatio-temporal resolution pan-African top-down biomass burning emissions made using

geostationary fire radiative power (FRP). In: And MAIAC Aerosol Optical Depth (AOD) Data. Remote Sensing of Environment, p. 248.
Omari, K., Abuelgasim, A., Alhebsi, K., 2019. Aerosol optical depth retrieval over the city of Abu Dhabi, United Arab Emirates (UAE) using Landsat-8 OLI images. Atmos. Pollut. Res. 10, 1075–1083.
Pacifici, F., Longbotham, N., Emery, W.J., 2014. The Importance of Physical Quantities for the Analysis of Multitemporal and Multiangular Optical Very High Spatial Resolution Images. IEEE Trans. Geosci. Remote Sens. 52, 6241–6256.
Pan, Y.F., Yang, J.S., Wang, J., Xu, G.J., Zheng, G., Chang, J.F., Gong, B., & Li, L.H. (2011). Investigation of typhoons by using ECMWF re-analysis data. In, *7th Symposium on Multispectral Image Processing and Pattern Recognition (MIPPR) - Remote Sensing Image Processing, Geographic Information Systems, and Other Applications*. Guilin, Peoples R China.
Rahman, H., Pinty, B., Verstraete, M.M., 1993a. Coupled surface-atmosphere reflectance (CSAR) Model.2. Semiempirical surface model usable with NOAA advanced very high-resolution radiometer data. J. Geophys. Res.-Atmos. 98, 20791–20801.
Rahman, H., Verstraete, M.M., Pinty, B., 1993b. Coupled surface-atmosphere reflectance (CSAR) MODEL.1. Model description and inversion on synthetic data. J. Geophys. Res.-Atmos. 98, 20779–20789.
Ramanathan, V., Crutzen, P.J., Kiehl, J.T., Rosenfeld, D., 2001. Atmosphere - Aerosols, climate, and the hydrological cycle. Science 294, 2119–2124.
Roman, M.O., Gatebe, C.K., Schaaf, C.B., Poudyal, R., Wang, Z.S., King, M.D., 2011. Variability in surface BRDF at different spatial scales (30 m-500 m) over a mixed agricultural landscape as retrieved from airborne and satellite spectral measurements. Remote Sens. Environ. 115, 2184–2203.
Roy, D.P., Zhang, H.K., Ju, J., Gomez-Dans, J.L., Lewis, P.E., Schaaf, C.B., Sun, Q., Li, J., Huang, H., Kovalskyy, V., 2016. A general method to normalize Landsat reflectance data to nadir BRDF adjusted reflectance. Remote Sens. Environ. 176, 255–271.
Samet, J.M., Dominici, F., Curriero, F.C., Coursac, I., Zeger, S.L., 2000. Fine particulate air pollution and mortality in 20 US Cities, 1987–1994. N. Engl. J. Med. 343, 1742–1749.
Sayer, A.M., Munchak, L.A., Hsu, N.C., Levy, R.C., Bettenhausen, C., Jeong, M.J., 2014. MODIS Collection 6 aerosol products: Comparison between Aqua's e-Deep Blue, Dark Target, and "merged" data sets, and usage recommendations. J. Geophys. Res.-Atmos. 119, 13965–13989.
Sayer, A.M., Hsu, N.C., Lee, J., Kim, W.V., Dutcher, S.T., 2019. Validation, Stability, and Consistency of MODIS Collection 6.1 and VIIRS Version 1 Deep Blue Aerosol Data Over Land. J. Geophys. Res.-Atmos. 124, 4658–4688.
Shang, P., Shen, F., 2016. Atmospheric Correction of Satellite GF-1/WFV Imagery and Quantitative Estimation of Suspended Particulate Matter in the Yangtze Estuary. Sensors 16.
She, L., Xue, Y., Guang, J., Mei, L.L., Che, Y.H., Li, Y., Fan, C., & Ieee (2017). AEROSOL OPTICAL AND PHYSICAL PROPERTIES OVER BEIJING. In, *IEEE International Geoscience & Remote Sensing Symposium* (pp. 5962-5965). Fort Worth, TX.
Shi, Q.J., Cao, G.Z., 2020. Urban spillover or rural industrialisation: Which drives the growth of Beijing Metropolitan Area. Cities 105.
Shi, Z., Li, Z.Q., Hou, W.Z., Mei, L.L., Sun, L., Jia, C., Zhang, Y., Li, K.T., Xu, H., Liu, Z.H., Ge, B.Y., Hong, J., Qiao, Y.L., 2022. Aerosol Optical Depth Retrieval Based on Neural Network Model Using Polarized Scanning Atmospheric Corrector (PSAC) Data. IEEE Trans. Geosci. Remote Sens. 60.
Shuai, Y.M., Schaaf, C.B., Strahler, A.H., Liu, J.C., Jiao, Z.T., 2008. Quality assessment of BRDF/albedo retrievals in MODIS operational system. Geophys. Res. Lett. 35.
Solheim, I., Engelsen, O., Hosgood, B., Andreoli, G., 2000. Measurement and modeling of the spectral and directional reflection properties of lichen and moss canopies. Remote Sens. Environ. 72, 78–94.
Sorek-Hamer, M., Kloog, I., Koutrakis, P., Strawa, A.W., Chatfield, R., Cohen, A., Ridgway, W.L., Broday, D.M., 2015. Assessment of PM2.5 concentrations over bright surfaces using MODIS satellite observations. Remote Sens. Environ. 163, 180–185.
Su, X., Wang, L.C., Zhang, M., Qin, W.M., Bilal, M., 2021. A High-Precision Aerosol Retrieval Algorithm (HiPARA) for Advanced Himawari Imager (AHI) data: Development and verification. Remote Sensing Environ. 253.
Sun, K., Chen, X.L., Zhu, Z.M., Zhang, T.H., 2017. High Resolution Aerosol Optical Depth Retrieval Using Gaofen-1 WFV Camera Data. Remote Sens. (Basel) 9.
Sun, L., Sun, C.K., Liu, Q.H., Zhong, B., 2010. Aerosol optical depth retrieval by HJ-1/CCD supported by MODIS surface reflectance data. Science China-Earth Sciences 53, 74–80.
Sun, L., Wei, J., Bilal, M., Tian, X.P., Jia, C., Guo, Y.M., Mi, X.T., 2016. Aerosol Optical Depth Retrieval over Bright Areas Using Landsat 8 OLI Images. Remote Sens. (Basel) 8.
Sun, M.X., Yu, L.J., Zhang, P., Sun, Q.Q., Jiao, X., Sun, D.F., Lun, F., 2021. Coastal water bathymetry for critical zone management using regression tree models from Gaofen-6 imagery. Ocean Coast. Manag. 204.
Tian, X.P., Liu, Q., Song, Z.W., Dou, B.C., Li, X.H., 2018. Aerosol Optical Depth Retrieval From Landsat 8 OLI Images Over Urban Areas Supported by MODIS BRDF/Albedo Data. IEEE Geosci. Remote Sens. Lett. 15, 976–980.
Urban, A., Di Napoli, C., Cloke, H.L., Kysely, J., Pappenberger, F., Sera, F., Schneider, R., Vicedo-Cabrera, A.M., Acquaotta, F., Ragettli, M.S., Iniguez, C., Tobias, A., Indermitte, E., Orru, H., Jaakkola, J.J.K., Ryti, N.R.I., Pascal, M., Huber, V., Schneider, A., de' Donato, F., Michelozzi, P., Gasparrini, A., 2021. Evaluation of the ERA5 reanalysis-based Universal Thermal Climate Index on mortality data in Europe. Environ. Res. 198.
van Donkelaar, A., Martin, R.V., Brauer, M., Kahn, R., Levy, R., Verduzco, C., Villeneuve, P.J., 2010. Global Estimates of Ambient Fine Particulate Matter Concentrations from Satellite-Based Aerosol Optical Depth: Development and Application. Environ. Health Perspect. 118, 847–855.
Vermote, E.F., Tanre, D., Deuze, J.L., Herman, M., Morcrette, J.J., 1997. Second Simulation of the Satellite Signal in the Solar Spectrum, 6S: An overview. IEEE Trans. Geosci. Remote Sens. 35, 675–686.
Wang, D.L., 2013. Study on the Problems of the Beijing's Financial Ecology. In: 3rd International Conference on Logistics, Informatics and Service Science (LISS). Beijing Jiaotong Univ, Sch Econ & Management, Reading, England, pp. 953–957.
Wang, F., Carmichael, G.R., Wang, J., Chen, B., Huang, B., Li, Y.G., Yang, Y.J., Gao, M., 2022. Circulation-regulated impacts of aerosol pollution on urban heat island in Beijing. Atmos. Chem. Phys. 22, 13341–13353.
Wang, D.D., Chen, Y.H., Zhan, W.F., 2018. A geometric model to simulate thermal anisotropy over a sparse urban surface (GUTA-sparse). Remote Sens. Environ. 209, 263–274.
Wang, M., Cheng, Y.F., Guo, B.B., Jin, S.Y., 2019a. Parameters determination and sensor correction method based on virtual CMOS with distortion for the GaoFen6 WFV camera. ISPRS J. Photogramm. Remote Sens. 156, 51–62.
Wang, M., Guo, B.B., Zhu, Y., Cheng, Y.F., Nie, C.H., 2019b. On-Orbit Calibration Approach Based on Partial Calibration-Field Coverage for the GF-1/WFV Camera. Photogramm. Eng. Remote Sens. 85, 815–827.
Wang, Z.X., Liu, Y., Hu, M., Pan, X.C., Shi, J., Chen, F., He, K.B., Koutrakis, P., Christiani, D.C., 2013. Acute health impacts of airborne particles estimated from satellite remote sensing. Environ. Int. 51, 150–159.
Wanner, W., Strahler, A.H., Hu, B., Lewis, P., Muller, J.P., Li, X., Schaaf, C.L.B., Barnsley, M.J., 1997. Global retrieval of bidirectional reflectance and albedo over land from EOS MODIS and MISR data: Theory and algorithm. J. Geophys. Res.-Atmos. 102, 17143–17161.
Wei, J., Huang, B., Sun, L., Zhang, Z., Wang, L., Bilal, M., 2017a. A Simple and Universal Aerosol Retrieval Algorithm for Landsat Series Images Over Complex Surfaces. J. Geophys. Res. Atmos. 122, 13,338–313,355.
Wei, J., Huang, B., Sun, L., Zhang, Z.Y., Wang, L.C., Bilal, M., 2017b. A Simple and Universal Aerosol Retrieval Algorithm for Landsat Series Images Over Complex Surfaces. J. Geophys. Res.-Atmos. 122, 13338–13355.
Wei, J., Li, Z.Q., Peng, Y.R., Sun, L., Yan, X., 2019. A Regionally Robust High-Spatial-Resolution Aerosol Retrieval Algorithm for MODIS Images Over Eastern China. IEEE Trans. Geosci. Remote Sens. 57, 4748–4757.
Witek, M.L., Garay, M.J., Diner, D.J., Smirnov, A., 2019. Oceanic Aerosol Loading Derived From MISR's 4.4 km (V23) Aerosol Product. J. Geophys. Res.-Atmos. 124, 10154–10174.
Wong, M.S., Nichol, J., Lee, K.H., Li, Z.Q., 2009. High resolution aerosol optical thickness retrieval over the Pearl River Delta region with improved aerosol modelling. Sci. China. Ser. D Earth Sci. 52, 1641–1649.
Wong, M.S., Lee, K.H., Nichol, J.E., Li, Z.Q., 2010. Retrieval of Aerosol Optical Thickness Using MODIS 500 x 500 m(2), a Study in Hong Kong and the Pearl River Delta Region. IEEE Trans. Geosci. Remote Sens. 48, 3318–3327.
Wong, M.S., Nichol, J.E., Lee, K.H., 2011. An operational MODIS aerosol retrieval algorithm at high spatial resolution, and its application over a complex urban region. Atmos. Res. 99, 579–589.
Wu, J.S., Yao, F., Li, W.F., Si, M.L., 2016. VIIRS-based remote sensing estimation of ground-level PM2.5 concentrations in Beijing-Tianjin-Hebei: A spatiotemporal statistical model. Remote Sens. Environ. 184, 316–328.
Wu, J.S., Liang, J.T., Zhou, L.G., Yao, F., Peng, J., 2019. Impacts of AOD Correction and Spatial Scale on the Correlation between High-Resolution AOD from Gaofen-1 Satellite and In Situ PM2.5 Measurements in Shenzhen City, China. Remote Sens. (Basel) 11.
Wu, Q.Z., Wang, Z.F., Gbaguidi, A., Gao, C., Li, L.N., Wang, W., 2011. A numerical study of contributions to air pollution in Beijing during CAREBeijing-2006. Atmos. Chem. Phys. 11, 5997–6011.
Xiao, Y., Hu, M., Zong, T.M., Wu, Z.J., Tan, T.Y., Zhang, Z.R., Fang, X., Chen, S.Y., Guo, S., 2021. Insights into aqueous-phase and photochemical formation of secondary organic aerosol in the winter of Beijing. Atmos. Environ. 259.
Xu, K., Zhang, G., Deng, M.J., Zhang, Q.J., Li, D.R., 2018. Improving Geometric Performance for Imagery Captured by Non-Cartographic Optical Satellite: A Case Study of GF-1 WFV Imagery. Remote Sens. (Basel) 10.
Yang, F.K., Fan, M., Tao, J.H., 2021. An Improved Method for Retrieving Aerosol Optical Depth Using Gaofen-1 WFV Camera Data. Remote Sens. (Basel) 13.
Yang, J., Shuai, Y.M., Duan, J.B., Xie, D.H., Zhang, Q.L., Zhao, R.S., 2022a. Impact of BRDF Spatiotemporal Smoothing on Land Surface Albedo Estimation. Remote Sens. (Basel) 14.
Yang, Y., Yang, K.Z., Chen, Y.P., 2022b. Aerosol Retrieval Algorithm for Sentinel-2 Images Over Complex Urban Areas. IEEE Trans. Geosci. Remote Sens. 60.
Yang, A.X., Zhong, B., Lv, W.B., Wu, S.L., Liu, Q.H., 2015. Cross-Calibration of GF-1/WFV over a Desert Site Using Landsat-8/OLI Imagery and ZY-3/TLC Data. Remote Sens. (Basel) 7, 10763–10787.
Yang, A.X., Zhong, B., Hu, L.F., Wu, S.L., Xu, Z.P., Wu, H.B., Wu, J.J., Gong, X.S., Wang, H.B., Liu, Q.H., 2020. Radiometric Cross-Calibration of the Wide Field View Camera Onboard GaoFen-6 in Multispectral Bands. Remote Sens. (Basel) 12.
Zhang, X., Chen, N.C., 2016. Reconstruction of GF-1 Soil Moisture Observation Based on Satellite and In Situ Sensor Collaboration Under Full Cloud Contamination. IEEE Trans. Geosci. Remote Sens. 54, 5185–5202.
Zhang, Y., Liu, Z.H., Wang, Y.Q., Ye, Z.X., Leng, L., 2014. Inversion of Aerosol Optical Depth Based on the CCD and IRS Sensors on the HJ-1 Satellites. Remote Sens. (Basel) 6, 8760–8778.
Zhang, Y., Li, Z.Q., Liu, Z.H., Zhang, J., Qie, L.L., Xie, Y.S., Hou, W.Z., Wang, Y.Q., Ye, Z.X., 2018b. Retrieval of the Fine-Mode Aerosol Optical Depth over East China Using a Grouped Residual Error Sorting (GRES) Method from Multi-Angle and Polarized Satellite Data. Remote Sens. (Basel) 10.

Zhang, J.F., Mauzerall, D.L., Zhu, T., Liang, S., Ezzati, M., Remais, J.V., 2010. Environmental health in China: progress towards clean air and safe water. Lancet 375, 1110–1119.
Zhang, T.H., Wang, L.C., Zhao, B., Gu, Y., Wong, M.S., She, L., Xia, X.H., Dong, J.D., Ji, Y. X., Gong, W., Zhu, Z.M., 2022. A Geometry-Discrete Minimum Reflectance Aerosol Retrieval Algorithm (GeoMRA) for Geostationary Meteorological Satellite Over Heterogeneous Surfaces. IEEE Trans. Geosci. Remote Sens. 60.
Zhang, G., Xu, K., Huang, W.C., 2017. Auto-calibration of GF-1 WFV images using flat terrain. ISPRS J. Photogramm. Remote Sens. 134, 59–69.
Zhang, Z.Y., Xu, X.D., Qiao, L., Gong, D.Y., Kim, S.J., Wang, Y.J., Mao, R., 2018c. Numerical simulations of the effects of regional topography on haze pollution in Beijing. Sci. Rep. 8.
Zhang, L.N., Yang, C.Y., Xiao, Q.Y., Geng, G.N., Cai, J., Chen, R.J., Meng, X., Kan, H.D., 2021. A Satellite-Based Land Use Regression Model of Ambient NO2 with High Spatial Resolution in a Chinese City. Remote Sens. (Basel) 13.
Zhang, H., Zhang, B., Chen, D.M., Li, J.S., Zhao, G.N., 2013. Influence of Filter Band Function on Retrieval of Aerosol Optical Depth from Sunphotometer Data. J. Atmos. Oceanic Tech. 30, 929–941.
Zhang, T.H., Zhu, Z.M., Gong, W., Zhu, Z.R., Sun, K., Wang, L.C., Huang, Y.S., Mao, F.Y., Shen, H.F., Li, Z.W., Xu, K., 2018a. Estimation of ultrahigh resolution PM2.5 concentrations in urban areas using 160 m Gaofen-1 AOD retrievals. Remote Sens. Environ. 216, 91–104.
Zhao, H.J., Gui, K., Ma, Y.J., Wang, Y.F., Wang, Y.Q., Wang, H., Zheng, Y., Li, L., Zhang, L., Che, H.Z., Zhang, X.Y., 2021. Climatology and trends of aerosol optical depth with different particle size and shape in northeast China from 2001 to 2018. Sci. Total Environ. 763.
Zhao, B., Wang, Y., Gu, Y., Liou, K.N., Jiang, J.H., Fan, J.W., Liu, X.H., Huang, L., Yung, Y.L., 2019. Ice nucleation by aerosols from anthropogenic pollution. Nat. Geosci. 12, 602–607.
Zheng, Y., Hou, W.Z., Li, Z.Q., Xu, W.B., Liu, X.R., Yang, L.K., 2020. Seasonal change analysis of multispectral BRDF for different surface types. 7th Symposium on Novel Photoelectronic Detection Technology and Applications, Kunming, Peoples R China.
Zheng, J.Y., Huang, X., Sangondimath, S., Wang, J.W., Zhang, Z.B., 2021. Efficient and Flexible Aggregation and Distribution of MODIS Atmospheric Products Based on Climate Analytics as a Service Framework. Remote Sens. (Basel) 13.